

On optical flow techniques applied to breaking surges

Rui Shi, Xinqian Leng, Hubert Chanson^{*}

The University of Queensland, School of Civil Engineering, Brisbane, QLD 4072, Australia

ARTICLE INFO

Keywords:

Breaking surges
Unsteady turbulence
Air-water flow
Optical flow techniques
Roller region

ABSTRACT

Surface wave breaking is a challenging two-phase flow process which plays an important role in numerous physical processes. A highly-turbulent unsteady breaking surge was investigated experimentally in a large facility, and substantial aeration occurred in the roller. The application of three optical flow techniques (Lucas-Kanade, Horn-Schunck and Farnback) to the air-water region was tested. The results indicated that the Farnback technique provided most accurate results, although some misleading results could be obtained near the air-water boundaries of the roller. The bore generation by a rapid gate closure showed a highly-unsteady complicated velocity field, with substantial free-surface deformations, wave breaking and formation of large coherent structures before the surge detached from the gate. Further upstream, the surge propagated as a hydraulic jump in translation and the data showed a marked shear region with a recirculation zone above, showing air-water flow features comparable to stationary hydraulic jumps. The upper and lower bounds of air-water flow region yielded data implying an air-to-water velocity ratio about 4–5 for a Froude number $Fr_1 = 2.1$.

1. Introduction

In the field of monophasic flow measurements, limited works have been done using the optical flow technique. The optical flow may be defined as the apparent motion between consecutive images, and the physical meaning of the optical flow data depends on the projective nature of the moving objects in camera field of view. Quénot et al. [1] first applied the optical flow using dynamic programming to particle image velocimetry (PIV), obtaining a more accurate velocity field with improved spatial resolution. Further developments [2–4] compared the optical flow results to fluid mechanics measurements, validating the technique in incompressible turbulent flow, and yielding detailed velocity fields. Recently physics-based optical flow techniques were reviewed in the context of monophasic flows [5].

The optical flow approach is less well-known in the hydraulic engineering and multiphase flow communities, despite the intrinsic limitations of monophasic flow metrologies (ADV, LDA, PIV) in highly aerated flow. Some limited work was developed in steady air-water flows on stepped chutes [6–8]. Zhang and Chanson [8] experimentally validated the velocities obtained from the optical flow techniques using an intrusive dual-tip phase-detection probe in aerated stepped spillway flows.

Wave breaking at the surface of oceans, lakes and rivers, is a challenging two-phase flow process which plays an important role in

numerous physical processes. Owing to the complexity of the two-phase turbulence in a breaker, theoretical models of wave breaking have typically relied on simplifying assumptions related to the bulk characteristics of the flow [9]. The flow may be modelled as a mixing layer [10] or in analogy with a hydraulic jump [11,12]. The details of the turbulence structure are lost in such bulk approximations. The knowledge of the highly fluctuating and aerated roller region would bring fruitful insight in the dynamics of the breaking surge. The temporal evolution of this region is a pre-requisite to get a better description of the time-variations of the air bubble entrapment and energy dissipation [9]. Physical modelling could provide details of the wave breaking at the millimetric to sub-millimetric scales, although most works are restricted to clear-water conditions, e.g. beneath the initial free-surface or near the incipient conditions for breaking [13,14].

Breaking surges may be analysed theoretically, experimentally in laboratory and the field, and numerically. Analytical solutions have been developed based upon 1D solutions since [15,16]; and include Benjamin and Lighthill [17] and Peregrine [18] among a few. Numerical CFD computations are limited, with the exception of the works of Simon [19] in undular bores and Khezri [20] and Leng [21] in breaking surges. A pertinent review is Leng et al. [22]. Experimental studies were originally focused on the free-surface properties (Bazin 1965, [23,24]). Unsteady turbulence measurements were undertaken during the last 20 years, both in laboratory [13,14,25] and in field tidal bores [26,27].

^{*} Corresponding author. School of Civil Engineering, The University of Queensland, Brisbane, QLD 4072, Australia.
E-mail address: h.chanson@uq.edu.au (H. Chanson).

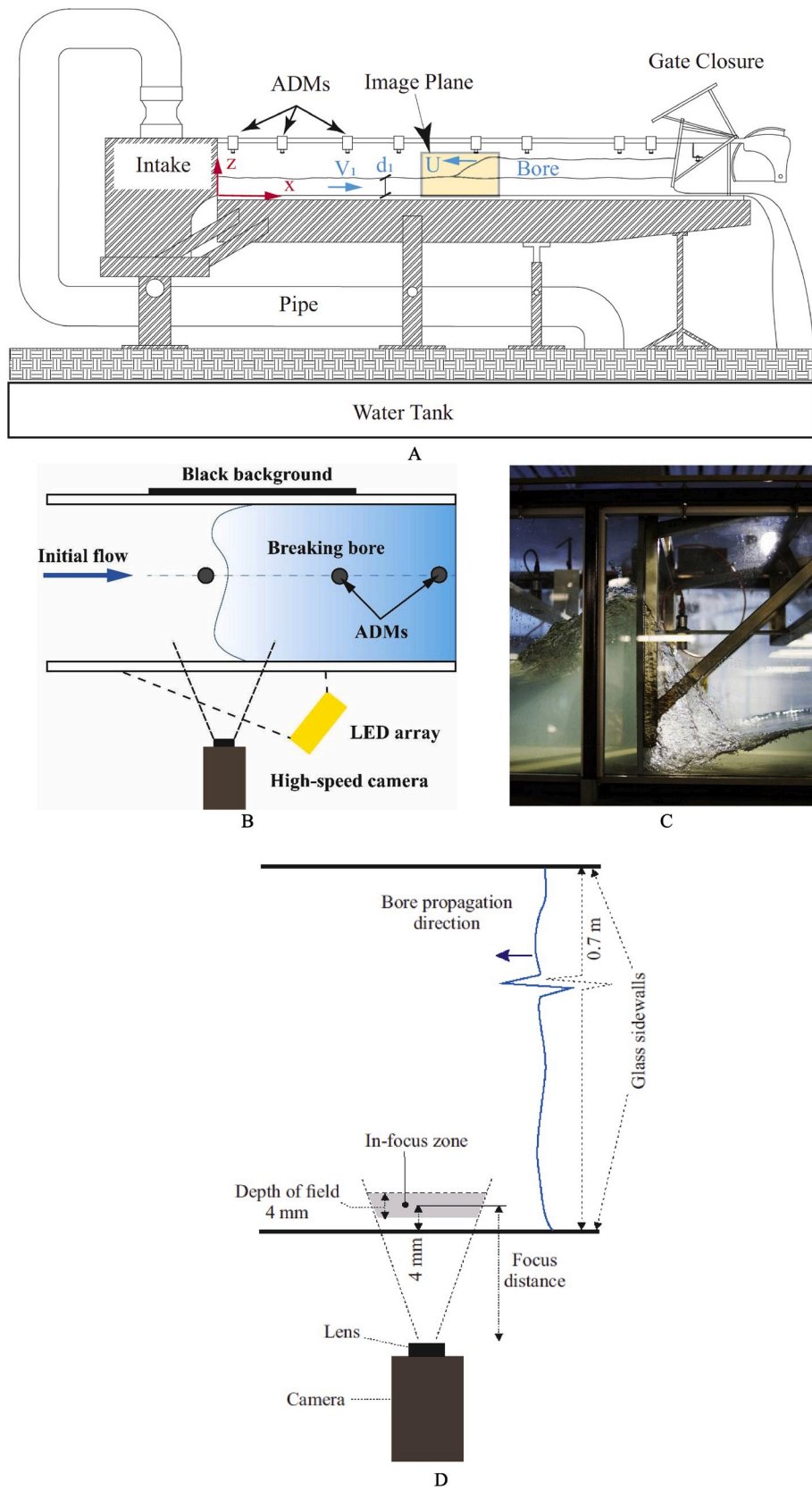


Fig. 1. Sketch and photographs of the experimental facility and breaking surge, with bore propagation from right to left - Flow conditions: $Q = 0.101 \text{ m}^3/\text{s}$, $Fr_1 = 2.1$, steady flow motion from left to right - (A) Distorted-sketch of the experimental facility; (B) Sketch of top view on experimental setup; (C) Side-view of the bore generation by rapid gate closure (shutter speed: $1/1000 \text{ s}$); (D) Details of the camera in-focus zone next to the sidewall, viewed in elevation.

Table 1
Key equations in three optical flow techniques.

description	Equation
BBC	$I(x_{im}, y_{im}, t_{im}) = I(x_{im} + dx_{im}, y_{im} + dy_{im}, t_{im} + dt_{im}) \quad (1)$
LK governing equation	$\begin{bmatrix} u_{im} \\ v_{im} \end{bmatrix} = \begin{bmatrix} \sum I_{x,i}^2 & \sum I_{x,i}I_{y,i} \\ \sum I_{x,i}I_{y,i} & \sum I_{y,i}^2 \end{bmatrix}^{-1} \begin{bmatrix} -\sum I_{x,i}I_{t,i} \\ -\sum I_{y,i}I_{t,i} \end{bmatrix} \quad (2)$
HS governing equation	$\iint (I_x u_{im} + I_y v_{im} + I_t)^2 + \alpha^2 (\ \nabla u_{im}\ ^2 + \ \nabla v_{im}\ ^2) dx_{im} dy_{im} \quad (3)$
FB governing equation	$d_f(x_{im}) = \left(\sum w_f A_f^T A_f \right)^{-1} \sum w_f A_f^T \Delta b_f \quad (4)$

Notes: BBC means brightness consistency constrains. Appendix A presents detailed illustrations of above equations.

Air-water flow measurements in breaking surges have only been conducted in the last few years [28,29].

It is the aim of the present study to investigate the application of optical flow techniques to the highly-turbulent air-water roller of unsteady breaking surge. This is achieved by applying different optical flow techniques and examining their performance in terms of angular error. The results delivers a novel, comprehensive characterisation of the turbulent two-dimensional velocity fields of the propagating breaking roller.

2. Experimental methods, facility and instrumentation

2.1. Experimental setup

A series of physical experiments were conducted in a 19 m long and 0.7 m wide rectangular tilting flume. The channel was made of glass sidewalls and smooth PVC bed. Fig. 1 shows sketches and photograph of the experimental facility and apparatus. The water discharge was supplied by two electronically controlled pumps, with the maximum discharge of 0.101 m³/s. The water initially passed an upstream intake tank equipped with baffles, flow straighteners and a smooth three-dimensional convergent. A fast closing Tainter gate was located at the downstream end of the channel at $x = 18.06$ m (Fig. 1C), where x is measured from the upstream end of the channel. The Tainter gate was rapidly closed to generate the positive surges propagating upstream. The duration of the gate closure was within 0.15 s to minimize any impact of the gate on the characteristics of the surges. Downstream of the gate, a free overfall discharged the water into an underground tank.

2.2. Instrumentation

The water discharge was measured by a magneto flow meter with an accuracy of 10⁻⁵ m³/s. The free surface profile and free surface fluctuations were measured non-intrusively using nine acoustic displacement meters (ADMs), including a MicrosonicTM Mic+35/IU/TC unit located immediately downstream of the Tainter gate at $x = 18.06$ m (seen in Fig. 1B) and eight MicrosonicTM Mic+25/IU/TC units located upstream of the Tainter gate at $x = 1.0$ m, 4.0 m, 7.0 m, 8.5 m, 10.0 m, 12.5 m, 16.5 m and 17.5 m. Their accuracies were within 0.18 mm. All the ADMs were mounted with the sensors above the channel centreline, facing towards the invert, and they were calibrated against point gauge measurements in steady flows, and sampled at 200 Hz.

Detailed breaking roller features and optical flow properties were recorded using a Phantom v2011 ultra-high-speed video camera, equipped with a Nikkor 50 mm f/1.4D lens. The camera was installed

beside the channel and recorded the air-water flow through the glass sidewall (Fig. 1B). The camera was able to record single-channel 12-bit images in full HD resolution of 1280 × 800 pixels with a maximum of 22,607 fps. The camera lens was set with a large aperture (f/1.4) and focused on the flow about 4 mm from the sidewall, with a depth of field (DOF) of 4 mm (Fig. 1D). A LED array (6 × 4 bulbs) provided the lighting on the experimental sampling location. The light intensity was modified by placing translucent light diffuser, to keep the light intensity as uniform as possible. The exposure time was adjusted to ensure adequate illumination throughout the videos. The high-speed video movies were transferred into 8-bits bitmaps for data analyses. The converted videos were post-processed using MATLAB to obtain the two-dimensional velocity field, shear layer and free surface profiles of the breaking roller (see below). The lens distortion of the images was checked and corrected by the Camera Calibration Toolbox implemented in MATLAB R2018a. Further flow patterns were photographed using digital cameras CasioTM EX-10 Exilim, AppleTM iPhone X, and a dSLR PentaxTM K-3.

3. Optical flow techniques and image processing algorithms

3.1. Presentation

The optical flow estimation, developed from computer vision scientists, is used to detect the apparent motion in the image plane that is induced by a projection of the objects in the three-dimensional space. The optical flow is based on the brightness constancy assumption that the image brightness intensity remains invariant along a sequence of images. The brightness equations are not directly derived from fluid-mechanics-based principles, and therefore the results obtained from the optical flow need to be validated against experimental results.

During the 1980s, many techniques for estimating optical flow have been proposed, mainly including four classes: the differential techniques [30–32], region-based matching techniques [33,34], energy-based techniques [35] and the phase-based techniques [36,37]. Barron et al. [38] evaluated the performance of these techniques and compared with the experimental results, indicating that the most reliable techniques were the local differential technique of Lucas and Kanade, and local phase-based technique of Fleet and Jepson.

From last two decades, the majority of start-of-art optical flow techniques are inspired from the original work of Horn and Schunck, so called variational techniques. They solved the energy minimization function with brightness data and spatial smoothness data. For these variational optical flow approaches, it is vital to separately talk about the function that formulates the brightness data (i.e. the technique), and the optimisation algorithm applied to minimize the assumptions in the

Table 2
Summary of the optical flow techniques.

Technique	Assumption	Pros	Cons
LK	Brightness constancy constraint Constant local optical flow fields Small displacement in motion	High robustness to noise	Non-dense flow fields
HS	Brightness constancy constraint Global smoothness constraint Small displacement in motion	Dense flow fields	Sensitive to noise
FB	Small displacement in motion	Relatively high accuracy, Dense flow fields	Over-smoothed flow field

function (i.e. the method). Although the governing formulations of these techniques have not been significantly updated, the accuracies continue to be improved by different optimisation methods, as presented by the Middlebury optical flow benchmark [39]. The coarse-to-fine methods are commonly used to compute large-displacement optical flow [40,41]. The high order constancy assumptions minimize the impact of luminance changes [42–44]. Spatial filtering and temporal filtering mechanics can remove electronic noise and impulse from the camera, extracting the global two-dimensional motion [45].

3.2. Optical flow techniques

In the present study, three optical flow techniques, namely the Horn-Schunck (HS) [30]; Lucas-Kanade (LK) [31] and Farneback (FB) [46,47] algorithms, were applied to obtain two-dimensional velocity fields in the highly aerated breaking surges. The reader is referred to Appendix A for more details about the three optical flow techniques.

Based on the approach of governing equations, the three techniques may be classified into (1) global technique that solve a minimization problem of the global energy functional, i.e. the HS technique, and (2) local approaches which assume a similar behaviour of the brightness intensity in a local neighbourhood and optimise energy-like expression, i.e. the LK and FB techniques [48]. The assumption within a neighbourhood in the local approaches (e.g. LK technique) enables a relatively high robustness to noise, but does not provide dense (pixel-by-pixel) optical flow fields. On the other hand, global approaches (e.g. HS technique) yield dense optical flow fields, but they are more sensitive to noise [38], because of the compromise between the regularisation parameter and details of the optical flow fields. The Farneback technique aims to combine the local and global approaches, by computing a dense optical flow field using adaptive polynomial coefficients in a local neighbourhood. The key equations of the three

techniques are listed in Table 1:

Both the LK and HS techniques are based on the brightness constancy constraint assumption, as illustrated in Equation (1) (Table 1). Additional constraints are required to address the indeterminacy of Equation (1). Lucas and Kanade [47] assumed small and constant displacement within local neighbourhood between two adjacent frames, and solved the optical flow fields by the linear least squares criterion. A key part is the invertibility of the system matrix in Equation (2) (Table 1). These local neighbourhoods with small eigenvalues of the system matrix result in non-dense optical flow fields. On the other hand, the single least criterion of the system matrix implicitly indicates a normal distribution of the image errors with a zero mean, implying a higher robustness to noise. Alternatively, Horn and Schunck [30] computed dense flow fields by proposing a smoothness constraint to formulate a minimiser of the global energy, (Equation (3), Table 1). The regularisation parameter α in Equation (3) is the ratio of the smooth errors to the errors in the brightness constancy constraint assumption, and its value needs to be carefully selected. A larger value of α leads to a more robust method for the large gradients of the brightness intensity, resulting in a smoother flow field. Further increase in the value of α will eventually address the large gradients due to image noise, but with some losses of details in the gradually varied gradient regions. A suitable regularisation parameter needs to consider both aspects, thus more sensitive to noise than the LK technique [38,48]. A clear advantage of the HS technique is the dense optical flow fields. The regularisation term in Equation (3) can fill the gap at the locations with the brightness constancy constraint term approximately equal to zero. The Farneback technique assumes slowly varied displacement field, resulting in an over-smoothed optical flow field. Its dense displacement field represents exact polynomial transforms of the brightness intensity, and is highly regarded in terms of accuracy and computational efficiency. Table 2 presents a brief summary of the three techniques.

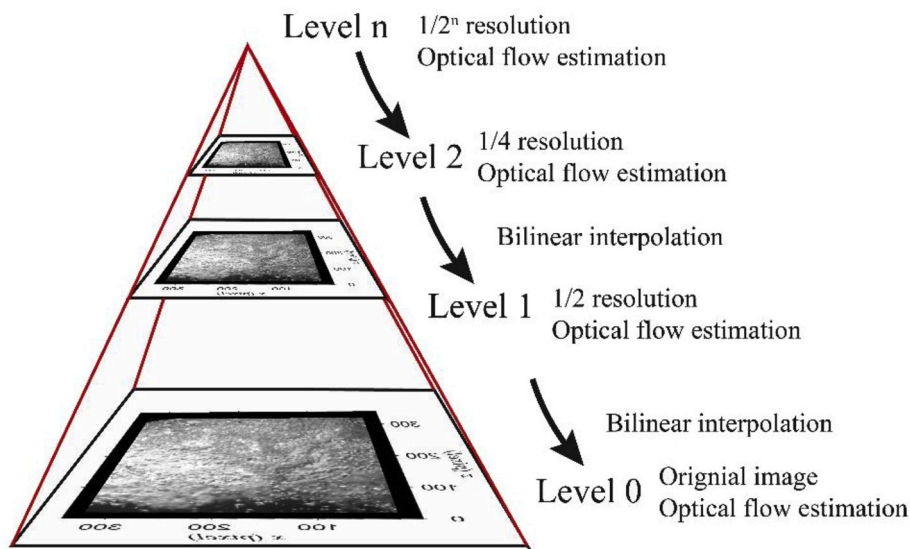


Fig. 2. Image pyramidal implementation.

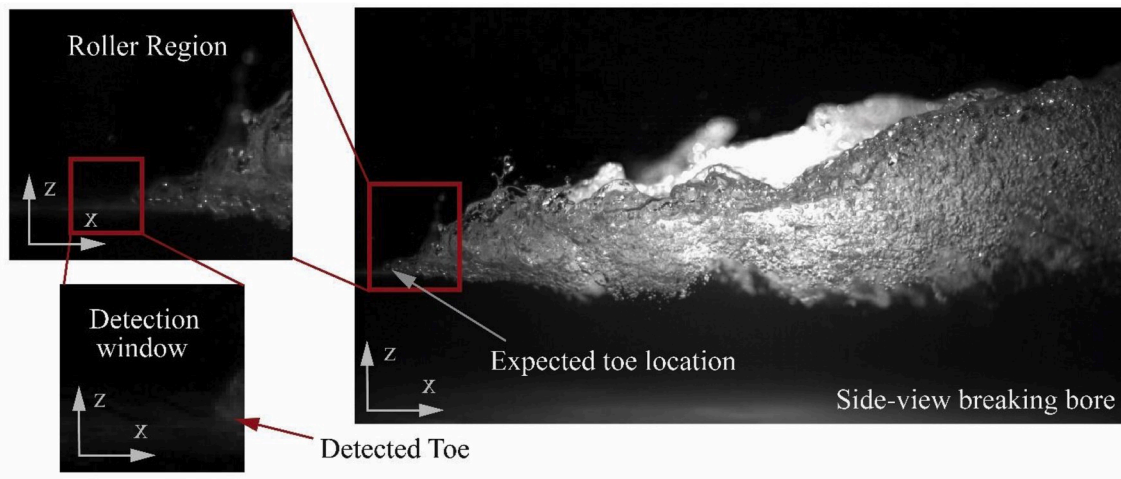


Fig. 3. Detection of the side-view high-speed video pictures - Initial flow from left to right, with breaking surge propagation from right to left - Flow conditions: $Q = 0.101 \text{ m}^3/\text{s}$, $Fr_1 = 2.1$, window size: 0.51 m long and 0.31 high.

All three optical flow techniques were combined with image pyramidal implementation to handle the large displacement. The pyramid is a multi-resolution method to repeatedly subsample and smooth the image. One of the common coarse-to-fine pyramids is the Gaussian pyramid. Fig. 2 presents the principle of multi-resolution pyramids. A pyramid scale was used to obtain an n-level pyramid. For example, if the scale is equal to 0.5, the image of the n-1 level of the pyramid is down-sampled to form the image of the n level of the pyramid, with the resolution reduced by half of the image of the preceding level. The optical flow algorithms were applied in the lowest resolution level to obtain initial vector field, which was bilinearly interpolated to act as the initial value of the new interactive refinement in the lower level. For detailed discussion on the image pyramid, the reader is referred to the works of Adelson et al. [42], Anderson et al. [49] and Burt [50,51].

In the present study, the brightness constancy constraint was assumed to be valid. Brightness variations however occurred during the passage of the breaking bores, thus resulting in certain inaccuracies of the optical flow. The different techniques were tested in terms of uncertainty by translating air-water flow images with a constant known

translation speed (section 6.1). The entire velocity field was thus known and the calculated flow fields were compared. To obtain a representative turbulent velocity field, an ensemble-averaged technique was applied to the optical flow results. One level of pyramid was selected to detect the large displacement herein, because of the ultra-high sampling rate (22,607 fps).

3.3. High-speed video synchronisation

The propagation of breaking bore is a highly turbulent and three-dimensional process. Owing to the turbulent nature, time-averaged unsteady flow properties are not meaningful in such highly turbulent flow, and the ensemble-averaged technique is adopted to characterise the flow properties. This subsection will introduce a novel algorithm on the synchronisation of the side-view high-speed video images, based upon the brightness intensity data, as illustrated in Fig. 3.

A novel approach has been to follow the bore roller, using the bore roller toe as reference. As a first step, all the images were shifted in such a fashion that the bore roller toe was always at the same (x, z) location in

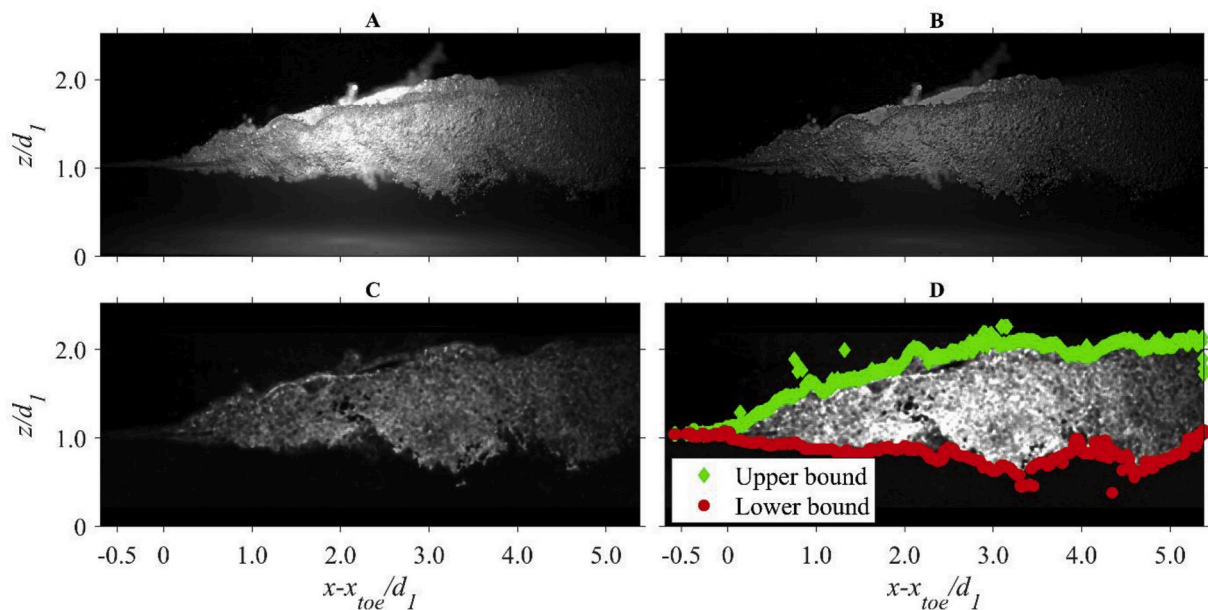


Fig. 4. Example of free surface detection algorithm - (A) original image from high-speed video; (B) new image obtained using subtraction of the original image and smoothed original image with a Gaussian kernel (C) filtered image gradients of image B; (D) detected free surface, with the original image plotted as a reference. Initial flow from left to right, with breaking surge propagation from right to left - Flow conditions: $Q = 0.101 \text{ m}^3/\text{s}$, $Fr_1 = 2.1$.

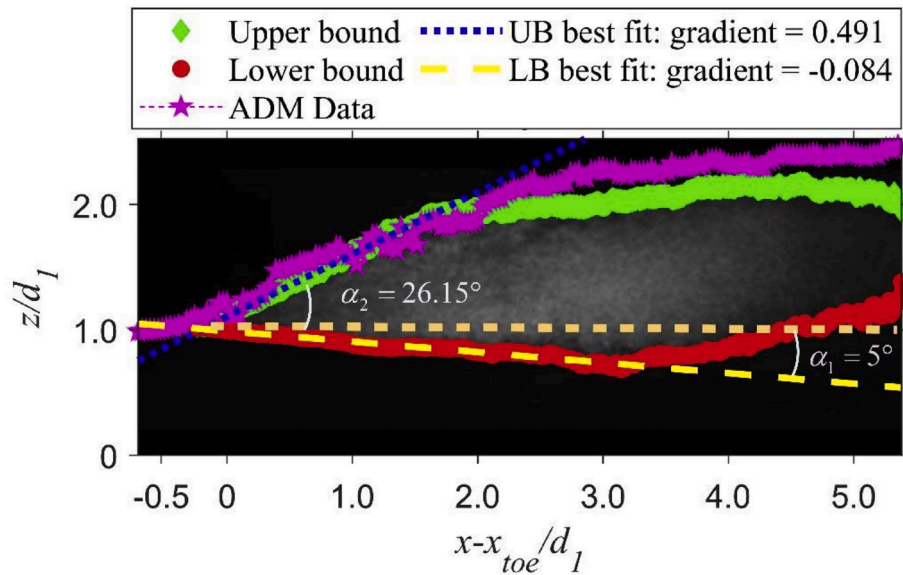


Fig. 5. Dimensionless ensemble-averaged boundaries of two-phase flow region in breaking bore, based on 23 videos. The image gradient data were plotted on the background as a reference. Comparison with ensemble-averaged acoustic displacement meter data recorded at $x = 8.5$ m. Note the outline of the air-water shear layer: dotted line for the upper bound (UB) and dashed line for the lower bound (LB).

the ‘synchronised’ images: i.e., it was located at the 150th pixel (origin at top-left corner) near the left-edge of the image planes (Fig. 3). A small detection window of 50×50 pixels was extracted from the image plane, with the left edge located at the 150th pixel. The bore arrival induced an increase in brightness intensity and spatial gradients in the detection window. The bore was detected based on a double threshold technique: (1) the sum of the brightness intensity of the first column in the detection window; and (2) the sum of the spatial gradient magnitude of the brightness intensity in the detection window:

$$\sum_{I_{im} \in W_{i,1}} I_{im} > C_{\text{threshold},1} \quad (5)$$

$$\sum_{I_{im} \in W_{i,j}} \sqrt{I_x^2 + I_y^2} > C_{\text{threshold},2} \quad (6)$$

where $W_{i,1}$ and $W_{i,j}$ are the first column and entire data set of the brightness intensity in the detection window respectively, $C_{\text{threshold},1}$ and $C_{\text{threshold},2}$ are constant values. The spatial brightness gradients were obtained using the Sobel operator:

$$I_x = I_{im} \begin{bmatrix} -1 & 0 & 1 \\ -2 & 0 & 2 \\ -1 & 0 & 1 \end{bmatrix} \quad \text{and} \quad I_y = I_{im} \begin{bmatrix} -1 & -2 & -1 \\ 0 & 0 & 0 \\ 1 & 2 & 1 \end{bmatrix} \quad (7)$$

The algorithm started with the first frame, and executed repeatedly until the bore front being detected. No adjustment of the two cut-off constants for different high-speed videos was required, because of the similar behaviour of the surge roller propagation and homogenous lighting condition. However, errors might be induced by an increase in the brightness intensity caused the reflection of the initial free-surface just before the bore arrival. The best solution was to manually check the synchronisation in the detection window.

3.4. Two-dimensional edge detection algorithm on air-water flow region-surfaces

A novel image-processing algorithm was developed to characterise the air-water roller region in the longitudinal and vertical plane. The algorithm aimed to detect the discontinuities in the image plane, at which the image data changed significantly because of the flow motion.

The algorithm included three parts. The first step was to subtract the

smoothed original image using a Gaussian smoothing (Appendix A) from the original image data to obtain a new image, as shown in Fig. 4. The purpose of this step was to remove the background information from the original image, minimising the effect of the out-of-plane motion on the two-dimensional free-surface detection. In the second step, the spatial brightness gradients of the new image were computed using the Sobel operator in Equation (7) and filtered by the Median Filter method. The latter removed the ‘salt and pepper’ noise that exhibited a Gaussian distribution over the image plane. Fig. 4C presents the outcome of the second step. In the third step, a single threshold technique was applied to detect the discontinuities of the filtered image gradient data. The upper and lower bounds of the air-water flow region are plotted in Fig. 4D, with the original image presented as a reference. The results showed that the detected edges represented well the boundaries of the air-water region in the breaking bore. Some droplets and entrained air bubble were detected, highlighted as small dots above and below the upper and lower bounds respectively.

Overall, the algorithm was able to extract physically-meaningful boundaries of the air-water flow region. The gradient-based edge detection algorithm however has several limitations. One concern was the subtraction of the Gaussian-smoothed original image data from the original image data which cannot remove all the background information, resulting in some overestimation of the edges of air-water flow region. Also the Median Filter Method interpolated relatively low value for the pixels near the edges, that might cause undetectable local neighbourhoods on the edge because of a decrease in the edge sharpness.

4. Visual observations and air-water flow boundaries

4.1. Presentation

The surges were characterised by their Froude number Fr_1 , set using different water discharges Q , small channel slope S_0 ($<1.5\%$) and Tainter gate opening h after closure. The Froude number of a surge is defined as: $Fr_1 = (V_1 + U)/(g d_1)^{1/2}$ where V_1 is the initial flow velocity positive downstream (Fig. 1), U is the bore translation speed positive upstream herein, g is the gravity acceleration and d_1 is the initial water depth. Visual observations suggested that the surge shape varied significantly from different Froude numbers. For Fr_1 less than unity, no bore was observed. Increasing Fr_1 between 1.05 and 1.15 led to an undular bore, characterised by a series of quasi two-dimensional

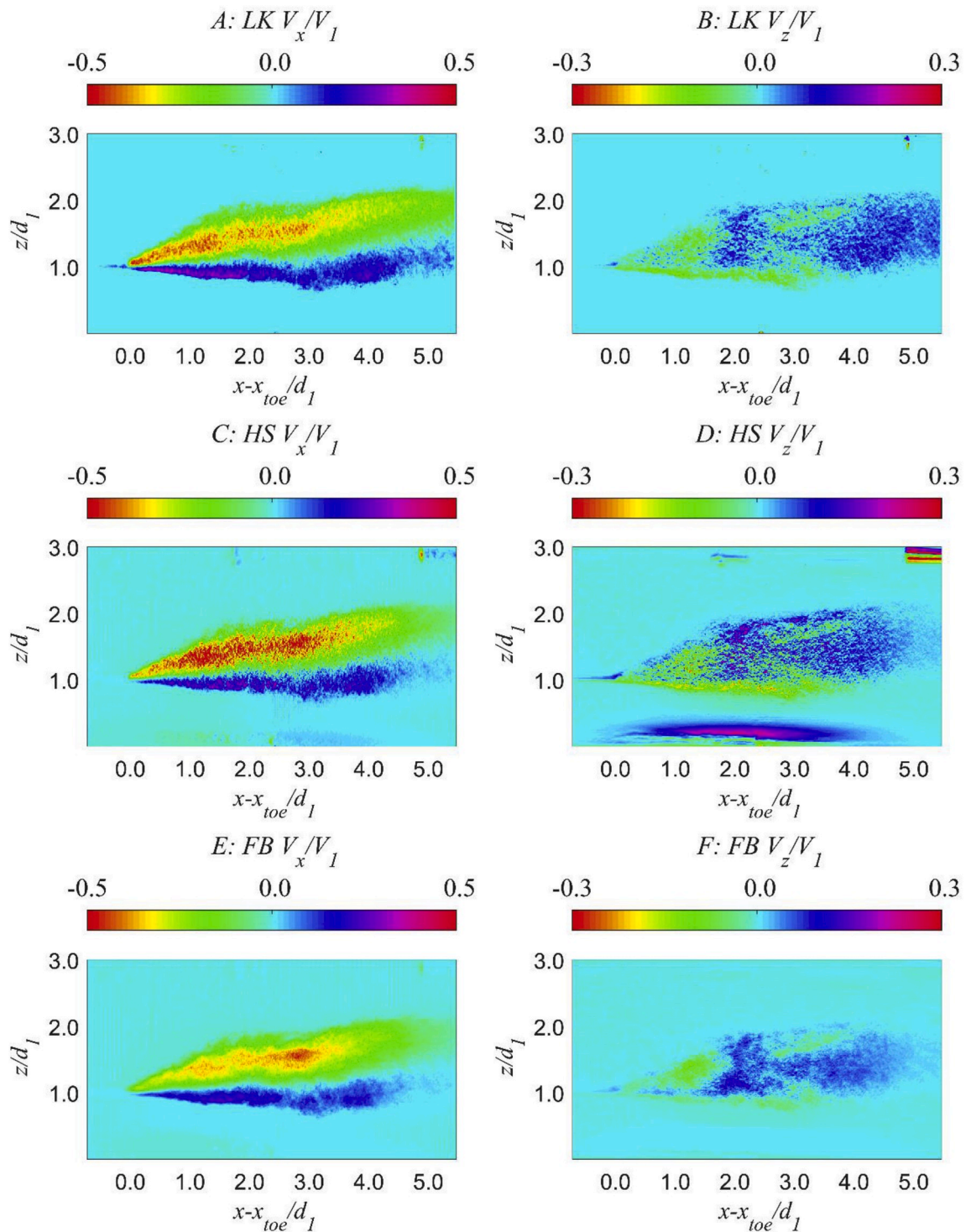


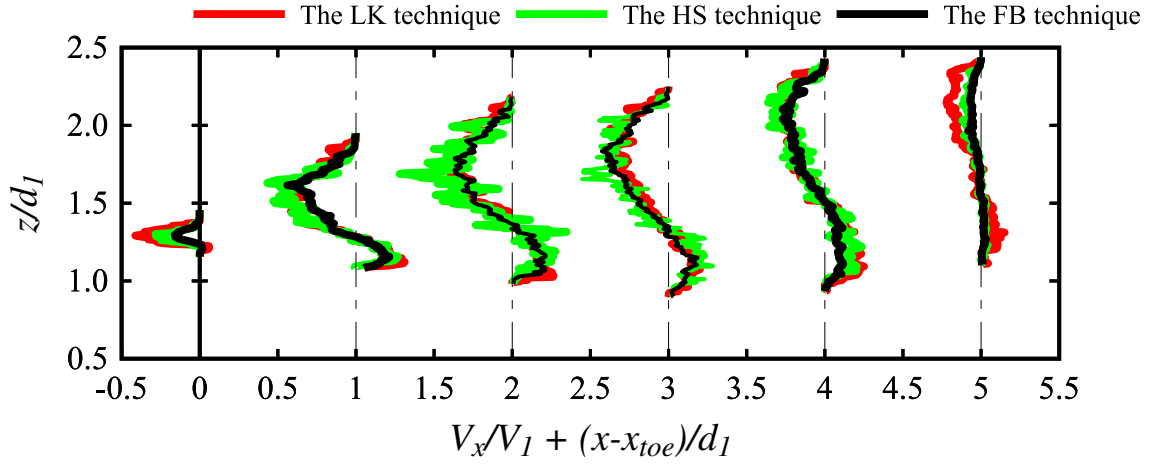
Fig. 6. Dimensionless ensemble-averaged instantaneous longitudinal and vertical optical flow velocity data using the LK, HS and FB techniques - Flow condition: initial flow from left to right, the bore propagation from right to left, $x = 8.5$ m, $Q = 0.101$ m³/s, $Fr_1 = 2.1$, 23 high-speed videos.

undulations with small amplitude and large wave length. For $1.15 < Fr_1 < 1.24$, the bore was still undular, but lateral shock waves developed from the channel sidewall. For $1.24 < Fr_1 < 1.40$, small breaking roller was developed at the first wave crest on the channel centreline, followed by a series of gentle and three-dimensional secondary waves. For Fr_1 larger than 1.40 and 1.60, the breaking roller was fully developed across the highly fluctuated bore front, with a rapid increase in the free surface and the free surface curved slightly upward in front of the bore front. Breaking bores with relatively high bore Froude number ($Fr_1 > 2$) were characterised by a highly aerated breaking roller, strong

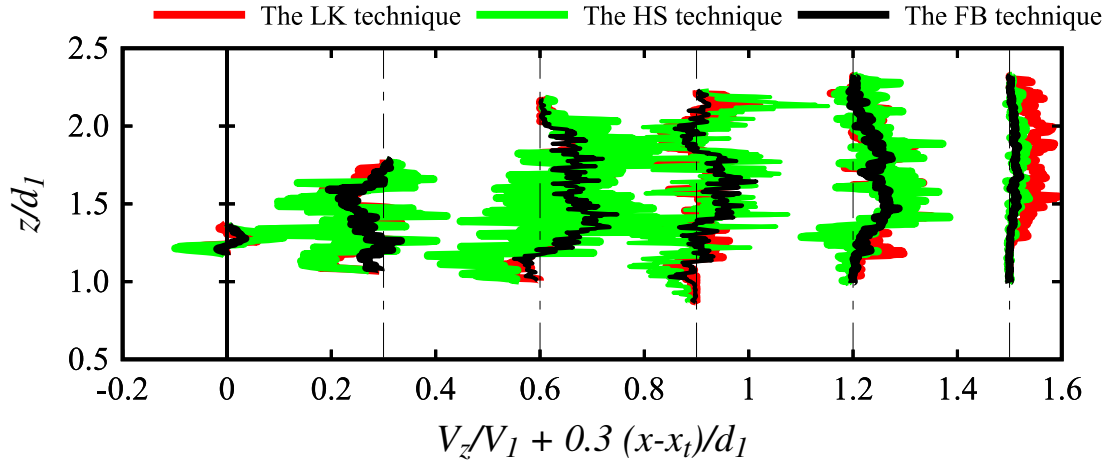
turbulent interactions and intense free-surface splashes at the bore front. Overall, the basic flow patterns were consistent with previous studies [13,52–55].

4.2. Air-water flow boundaries

The dimensionless ensemble-averaged boundaries of air-water flow region in the breaking surge are presented in Fig. 5, with the image gradient data plotted as a reference. The breaking surge characteristics were $Fr_1 = 2.1$ and $d_1 = 0.097$ m. The free surface profile, marked as the



A: Ensemble-averaged longitudinal velocity profiles



B: Ensemble-averaged vertical velocity profiles

Fig. 7. Ensemble-averaged instantaneous velocity profiles for different optical flow techniques at longitudinal locations: $x - x_{toe} = 0, 1.0, 2.0, 3.0, 4.0$ and 5.0 .

upper bound of the air-water region, showed that the breaking bore roller formed immediately downstream of the discontinuity in water level. With an increasing horizontal distance from the roller toe, the ensemble-averaged free surface data showed a relatively rapid increase in free-surface elevation up to $(x-x_{toe})/d_1 = 1.5$, followed by a slower rate raise to the conjugate depth at $(x-x_{toe})/d_1 = 4.0$. The free-surface profile data compared favourably with the ensemble-averaged acoustic displacement meter (ADM) data, although the latter was recorded at a fixed location on the channel centreline. The lower bound of the air-water roller region, formed at the roller toe, broadened the air-water flow region until $(x-x_{toe})/d_1 = 2.8$. The broadening of the air-water region immediately downstream of the breaking roller toe suggested a convective transport of entrained air bubbles in the turbulent shear layer. Further downstream, the lower bound of the air-water region tended to ascend towards the free surface, linked to the de-aeration process of the air-water region by buoyancy. For $0 < (x-x_{toe})/d_1 < 2.8$, the shape of the lower bound was consistent with the lower extent of the main shear layer in stationary hydraulic jump [56,57].

A key feature of the breaker surge was the spatially growing shear layer entraining an unequal amount of air and water in the roller itself. Based upon the geometrical properties of the large-scale air-water flow structures, the entrainment ratio and growth of the turbulent mixing may be argued [56,58]. From the ensemble-averaged data (Fig. 5), the upper and lower bounds of air-water flow region were best correlated by:

$$\frac{y_{UB}}{d_1} = 0.491 \frac{x - x_{toe}}{d_1} + 0.91 \quad 0 < \frac{x - x_{toe}}{d_1} < 1.5 \quad (8)$$

$$\frac{y_{LB}}{d_1} = -0.084 \frac{x - x_{toe}}{d_1} + 0.88 \quad 0 < \frac{x - x_{toe}}{d_1} < 1.5 \quad (9)$$

where x is the longitudinal distance measured from the upstream end of the channel, x_{toe} is the longitudinal distance of roller toe, d_1 is the initial water depth (Fig. 1A), y_{UB} and y_{LB} are the vertical distances of upper and lower bounds. Equations (8) and (9) are drawn in Fig. 5. In the present study, the two positive angles of shear-layer edges, denoted as α_1 and α_2 , were equal to 5° and 26.15° respectively. The data were close to the observations of Hoyt and Sellin [56] in a small-scale hydraulic jump without air entrainment. The volume-entrainment ratio may be defined as:

$$E_v = \frac{\tan \alpha_1}{r \tan \alpha_2} \quad (10)$$

where r is the ratio of air velocity to water velocity immediately prior to the roller toe [58]. Leng and Chanson [29] recorded the longitudinal variations of depth-averaged void fraction in the breaking surge. Their results showed a decreasing mean void fraction with increasing distance from the roller toe, and their data yielded a spatial-averaged volume-entrainment ratio E_v of 0.045 for $0 < (x-x_{toe})/d_1 < 1$ and 0.029 for $0 < (x-x_{toe})/d_1 < 1.5$. Based upon the observed shear-layer edges

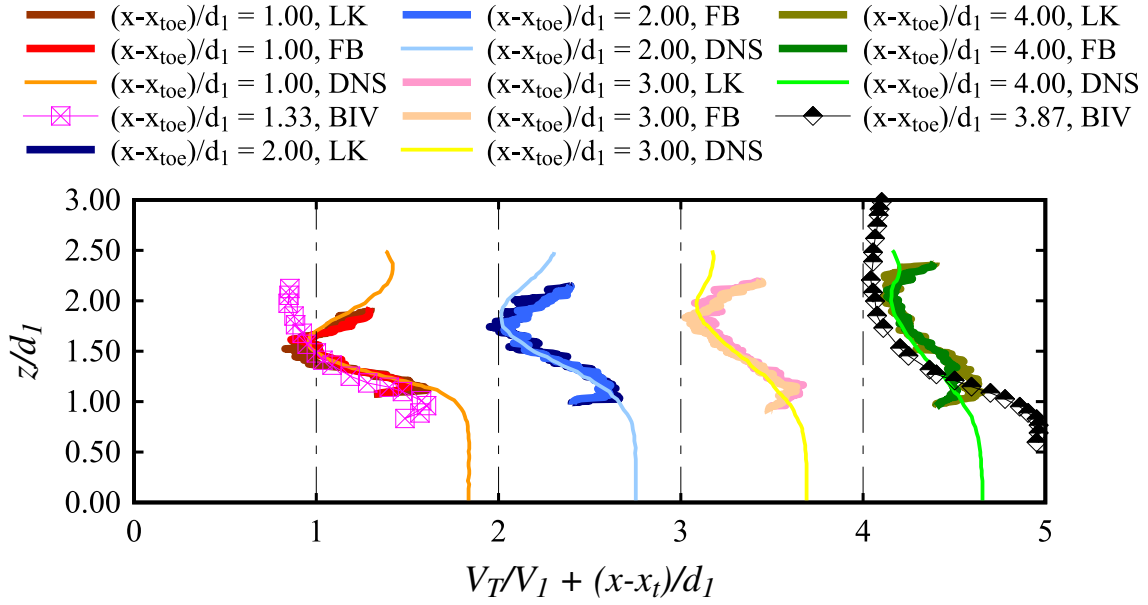


Fig. 8. Comparison of longitudinal velocity at longitudinal locations $x - x_{toe} = 1.0, 2.0, 3.0$ and 4.0 . DNS and BIV data were extracted from the works of Mortazavi et al. [60] and Lin et al. [61]; which presented hydraulic jump data with $Fr_1 = 2.0$ and 3.8 respectively.

(Fig. 5), Equation (10) would imply a ratio r of air velocity to water velocity before the bore of 3.75 – 5.75 . The entrainment ratio would be close to the square root of the freestream density ratio, as first proposed by Brown [59].

For completeness, the growth of the shear layer and entrainment ratio may be further related to the local ratio of large-coherent-structure spacing L_{eddy} to distance from the singularity $(x - x_{toe})$ [58].

5. Ensemble-averaged two-dimensional velocity fields

Observations using ultra-high speed video cameras through the glass sidewall were recorded for $Fr_1 = 2.1$. The experiments were repeated 23 times, enabling ensemble-averaged results. In each video, the sampling rate was 22,607 fps, and one pixel corresponded to 0.000391 m (0.391 mm/pixel). With a surge celerity of 0.7 m/s, the bore advanced by 0.03 mm in average between two consecutive frames. Visually, a detectable motion was observed for about every 100 frames (0.0044 s). Since an ultra-high sampling rate might increase the noise level, the instantaneous velocity was computed by averaging 100 frame-to-frame velocities. A sensitivity analysis indicated that the ensemble-averaged technique required at least 20 repetitions to obtain a reasonable smoothed velocity field in the breaking bores (Appendix C). The detailed sensitivity analysis is presented in the supplementary material. All runs were synchronised based upon the location of the breaking roller determined in terms of the brightness intensity data (Section 3.3). In the rest of this paper, the ensemble-averaged optical flow field were based on 23 videos.

5.1. Flow fields

A comparison of the results obtained from the three optical flow techniques was undertaken in the breaking bore at $x = 8.5$ m. A detailed comparison is presented in Fig. 6, where V_x and V_z are positive in the downstream and upward directions respectively, and V_1 is the initial flow velocity. For a given velocity field, the origin of the coordinate system was located at the roller toe, with x positive downstream and z positive upstream.

A number of common characteristics were observed with all methods. Overall all three optical flow techniques were able to compute detailed and smooth velocity fields in the two-phase flow and initial free-surface regions. Limited information was given in the clear water

regions, because of small variation in the brightness intensity. A similar bore front shape was observed, with water level above the roller toe ascending gradually to the conjugate depth. The velocity fields showed the same orders of magnitude, with V_x/V_1 and V_z/V_1 ranging from -0.5 to 0.5 and -0.3 to 0.3 respectively. The velocity distributions from the three techniques were in a good agreement globally, except for a few localised regions where the velocities fields were not consistent, e.g. the noise on the top and bottom of the vertical velocity field. The initial flow had constant longitudinal velocities of 0.5 m/s before the bore arrival, with a slight upward motion in front of the roller toe, highlighted as the small blue regions in front of the toe. The air-water shear regions, seen as the blue areas beneath the bore roller in the longitudinal velocity data, were well-defined. The leading edge of the surge roller experienced high absolute value of longitudinal velocities ($V_x/V_1 \approx -0.3$ to -0.4) and positive vertical velocities ($V_z/V_1 \approx 0.1$ to 0.2) within the roller regions, while low absolute value of the longitudinal velocities ($V_x/V_1 = -0.1$ to -0.2) and negative vertical velocities ($V_z/V_1 = -0.1$ to -0.2) were observed in the rest of the flow. The vertical velocity fields varied spatially in term of the direction, implying the presence of large vortices in the breaking rollers.

While a good agreement was seen in terms of the velocity fields among the three optical flow techniques, the HS technique provided some meaningless velocity data in the clear water region next to the channel bed, caused by the brightness intensity change induced by the bore passage. The presence of such misleading velocity data indicated that the HS technique was more sensitive to the change in the lighting condition than the other techniques, consistent with earlier discussions. Dense velocity fields obtained from the HS technique experienced larger regions of velocity discontinuity than the LK and FB techniques, possibly due to the fill-in-effect of the regularisation term in the HS technique dominating at the locations with almost zero brightness intensity gradients. On the other hand, the FB technique provided relatively smoother velocity fields. Overall the results suggested that the HS technique might be too noisy to use in the air-water flow region.

5.2. Quantitative comparison

The comparison of the longitudinal and vertical velocity profiles for the three optical flow techniques is presented in Fig. 7 at the different longitudinal locations, where the optical flow velocity is an air-water flow velocity. For the longitudinal velocity, all the profiles exhibited a

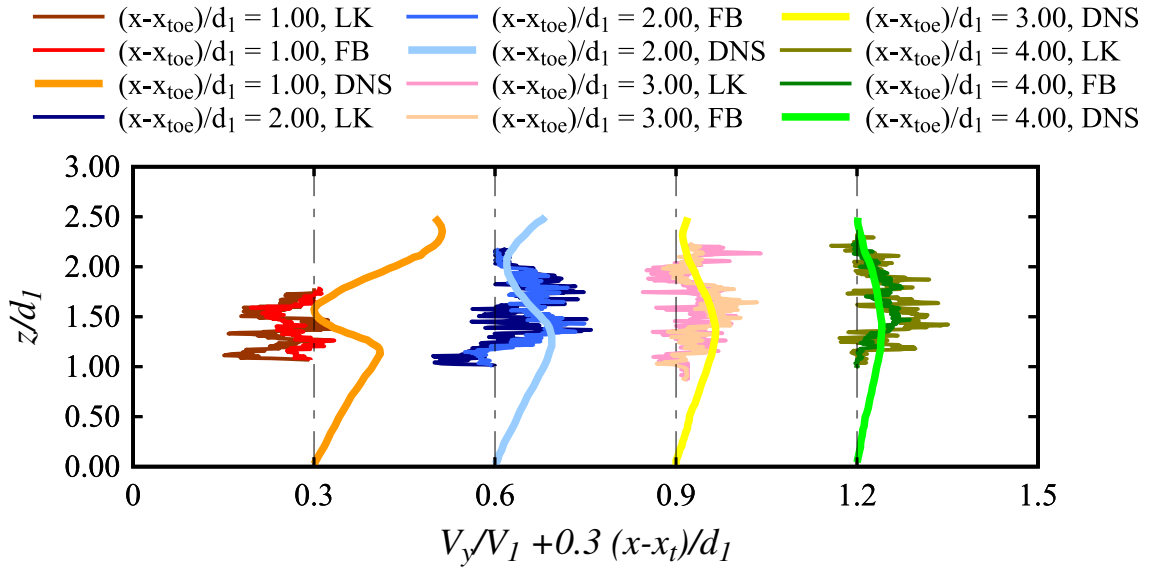


Fig. 9. Comparison of vertical velocity at longitudinal locations $x - x_{toe} = 1.0, 2.0, 3.0$ and 4.0 . DNS data were extracted from the works of Mortazavi et al. [60].

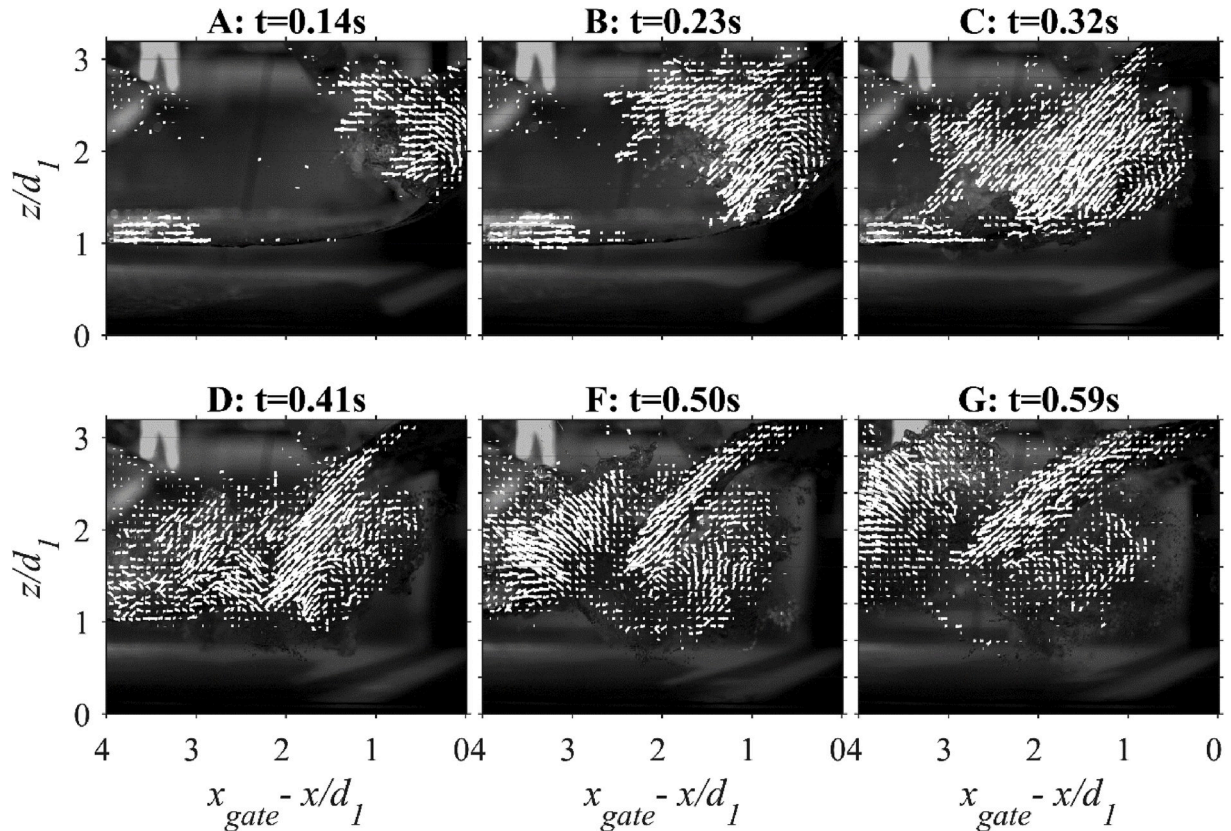


Fig. 10. Ensemble-averaged instantaneous two-dimensional optical flow velocity vectors using the FB technique for the bore generation process, with $t = 0$ was at the time when the Tainter gate was completely closed - Flow conditions: initial flow direction from left to right, bore propagation from right to left, $x = 18.0$ m, $Q = 0.101$ m³/s, $Fr_1 = 2.1$, 23 high-speed video movies. Note x_{gate} is longitudinal location of the gate at $x = 18.06$ m

self-similarity with S shape. Two pronounced peaks were observed: a positive peak in the lower shear layer and a negative peak above the propagating roller. With an increase in longitudinal distance from the roller toe, the self-similar shape tended to be flattened, with a decay in both peak values (Fig. 7). The longitudinal velocity profiles showed a good agreement for the three optical flow techniques, except for the toe location ($x - x_{toe} = 0$) and the edge of the image plane where was further away from the LED light ($x - x_{toe} = 5.0$). The HS technique gave noisy

velocity profiles, limited to the sensible nature of the HS technique. The FB technique computed relatively small velocity on the edge of the image plane, possible due to inadequate lighting. A comparison of the vertical velocity profiles showed similar performances of the three optical flow techniques. Overall the HS technique is considered too noisy in the present study, and not recommended to use in the air-water flow. The FB and LK techniques provided comparable results.

A literature review indicated some limited studies on velocity mea-

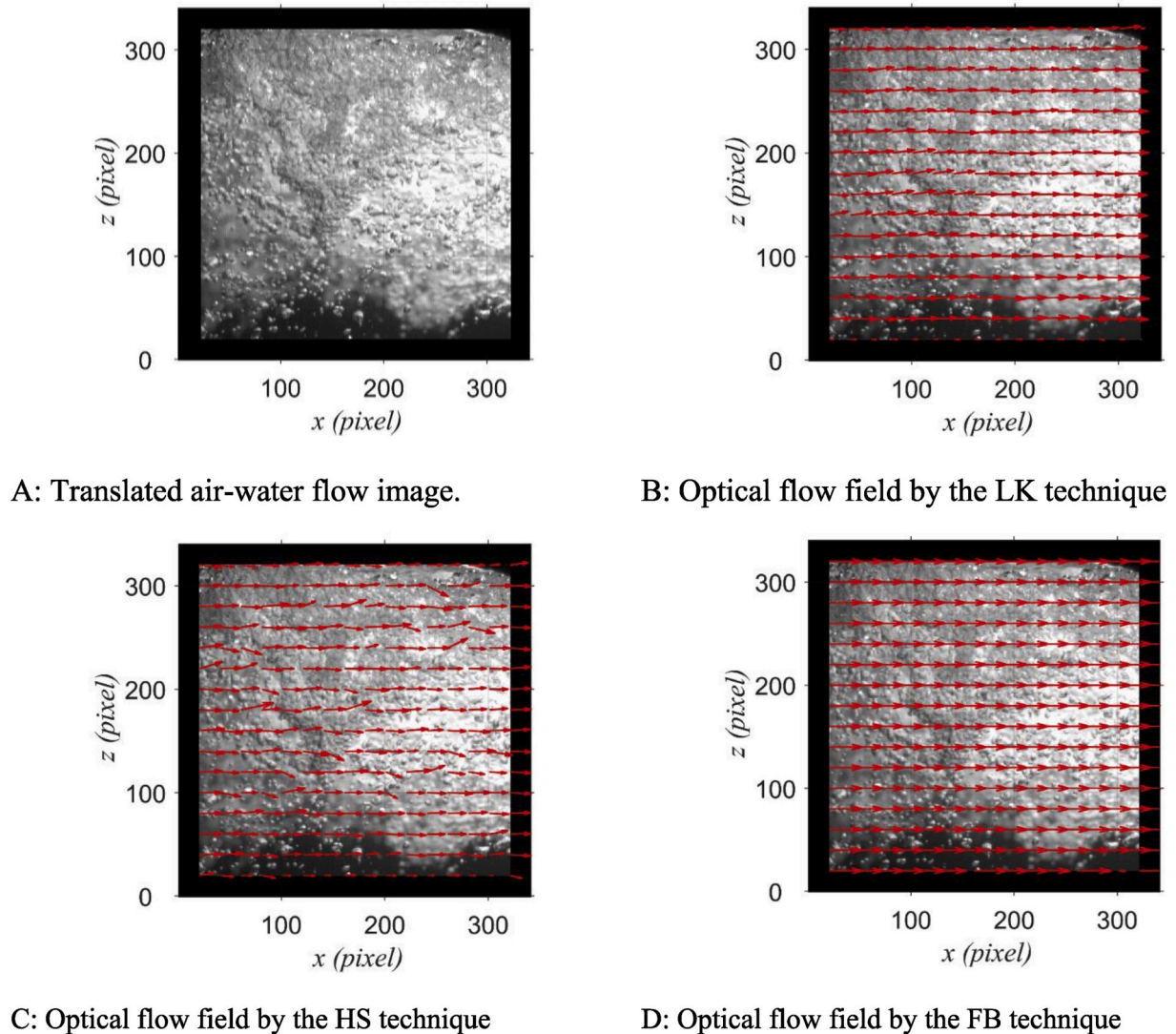


Fig. 11. Three optical flow techniques applied to air-water flow image.

measurements in the highly turbulent breaking surge roller, e.g. Hornung et al. [13] who used PIV to obtain limited turbulent characteristics. The present results were compared to stationary hydraulic jump data by translating present longitudinal velocity using bore celerity:

$$V_T = V_x - U \quad (11)$$

where U is the bore celerity measured using the ADMs. The translated longitudinal velocity profiles at different longitudinal locations from the LK and FB techniques are compared to direct numerical simulation (DNS) results on a hydraulic jump with $Fr_1 = 2.0$ [60] and bubble image velocimetry (BIV) data of a hydraulic jump with $Fr_1 = 4.51$ [61] in Fig. 8. Overall, the present results were consistent with the DNS simulation, except near the air-water flow boundaries, where the optical flows were misleading. The comparison with the data of Lin et al. [61] showed a qualitative agreement in terms of shape and self-similarity. The quantitative difference might be caused by the different methodology. The BIV technique detected the bubble motion based upon the correlation methods, whereas the optical flow technique detected the motion of brightness change.

The vertical velocity profiles were compared to the DNS data at different longitudinal velocity in Fig. 9, showing a reasonable agreement at the locations $x-x_{toe} = 2.0, 3.0$ and 4.0 . Some inconsistency was observed next to the roller toe ($x-x_{toe} = 1.0$). It is believed that the stationary hydraulic jump and translating breaking surge are not strictly

identical physical process, with differences in the roller toe properties.

In summary, the quantitative comparison indicated that the FB technique can be best used in the highly turbulent air-water flow, and no sidewall boundary effects were observed from the ensemble-averaged velocity profiles.

5.3. Bore generation process

The FB technique was used to investigate the bore generation process. The breaking bore was generated by a rapidly closing the Tainter gate at the downstream end of the channel. Fig. 10 presents the instantaneous ensemble-averaged two-dimensional optical flow velocity vectors at different instants t , with the photographs plotted in the background. In Fig. 10, $t = 0$ corresponds to the gate closure time, i.e. the complete gate closure when the gate's lower edge touched the invert. Note that the ensemble-averaged velocity vector fields might not match the photos in Fig. 10, since the bore generation was a highly turbulent process. The high-speed video movies were sampled at 22,607 fps, and were manually synchronised based upon the complete gate closure.

The optical flow data showed a great level of details during the bore generation. The initially steady flow impacted the gate at the time of closure ($t = 0$ s), and then piled upwards with a smooth curvature until reaching a height of approximately twice initial water depth ($t = 0.14$ s). The running-up water then splashed down ($t = 0.32$ s), forming a

Table 3

Key parameters of three optical flow techniques using a minimization of the angular error.

Technique	parameter	Value	Units
LK	window size (w)	22	pixel
HS	regularisation constant (α) in Equation (3)	2	(-)
FB	window size (w)	5	pixel

plunging jet with large air cavities at the impingement point ($t = 0.41$ s). The substantial free surface deformation induced the formation of large-scale vortices during the wave breaking. The entrained air cavities were enclosed during the formation of large coherent structures, before being broken up into small bubbles by the intense turbulence ($t = 0.51$ s and 0.59 s). The recirculation generated the breaking roller, which then detached from the gate and propagated upstream, as a breaking surge. The finding was overall consistent with, albeit much more detailed than, the CFD results of Lubin et al. [62] and the visual observations of Sun et al. [63] and Leng and Chanson [28,29].

6. Discussion on error and turbulence measurement

6.1. Measure of error

The error of the three optical flow techniques was examined using real air-water flow images. A random air-water image with 300 by 300 pixels was taken from a video, and moved horizontally by two pixels to the right (Fig. 11A). Note that Fig. 11A had a black margin width of 20 pixels around the original figures. The optical flows between the original and translated images were computed using the LK, HS and FB techniques (Fig. 11B–D). The velocity fields of the LK and FB techniques showed a horizontal movement, but the HS technique provided vertical velocities. Quantitatively, the angular errors were computed using the optical flow velocities and true velocities [39] as:

$$\psi_E = \cos^{-1} \left(\frac{1 + u_{im}u_{GT} + v_{im}v_{GT}}{\sqrt{1 + u_{im}^2 + v_{im}^2} \sqrt{1 + u_{GT}^2 + v_{GT}^2}} \right) \quad (12)$$

where u_{im} and v_{im} are the horizontal and vertical optical flows respectively, u_{GT} (2 pixels/frame) and v_{GT} (0 pixels/frame) are the true horizontal and vertical velocities respectively. A minimization of the angular error was used to set the key parameters of the three optical flow

techniques (Table 3). The detailed error analysis is presented in Appendix B. Fig. 12 presents the distributions of angular errors for the three optical flow techniques based on a uniform horizontal displacement of 2 pixels.

Overall, the results showed that the FB technique provided relatively smaller errors in the air-water flow with the average angular error across the whole image $\overline{\psi_E} = 10.86^\circ$, in comparison to $\overline{\psi_E} = 12.05^\circ$ and 15.78° for the LK and HS techniques respectively. Next to the boundary between the image and margin (Fig. 12), the brightness constancy constrain assumption was not valid, and large angular errors were observed. After removing these incorrect angular errors near the boundary, the $\overline{\psi_E}$ values of the FB, LK and HK techniques were 2.22° , 6.75° and 10.80° respectively. In summary, the FB technique yielded the smallest average angular error among the three techniques.

6.2. Turbulence measurements

Based on the instantaneous turbulent velocities in a breaking surge, the turbulence characteristics can be further derived. A question remains: how reliable will the turbulence characteristics be? The comparison and error analysis suggested that the optical flow techniques provided a good estimation on the averaged velocity fields, but instantaneous optical flow experienced a noise issue in the breaking roller (see the supplementary material), resulting in misleading turbulence properties. The optical flow techniques have their own limitations. The key assumption in the LK technique is a small and uniform displacement in a local neighbourhood of n pixels ($n = 22$ in the present study). In such case, turbulent structures with length scale smaller than the neighbourhood size will be neglected in the breaking roller. The LK technique obtains a non-dense velocity field, making impossible to compute accurate turbulence characteristics. The FB technique also uses small neighbourhoods because it is unlikely to assume a quadratic polynomial globally. The FB technique turns into a minimization problem in the neighbourhood, which can be the true turbulence motion of the brightness at each pixels, but completely depends on the quadratic relationship under translation. The HS technique provides a dense velocity field, but the noise issue became a challenge for the turbulence measurements.

In the highly turbulent breaking surge, the optical flow velocity is the air-water interfacial velocity. Therefore, the turbulence measurements may be affected by the brightness change induced by the air bubbles

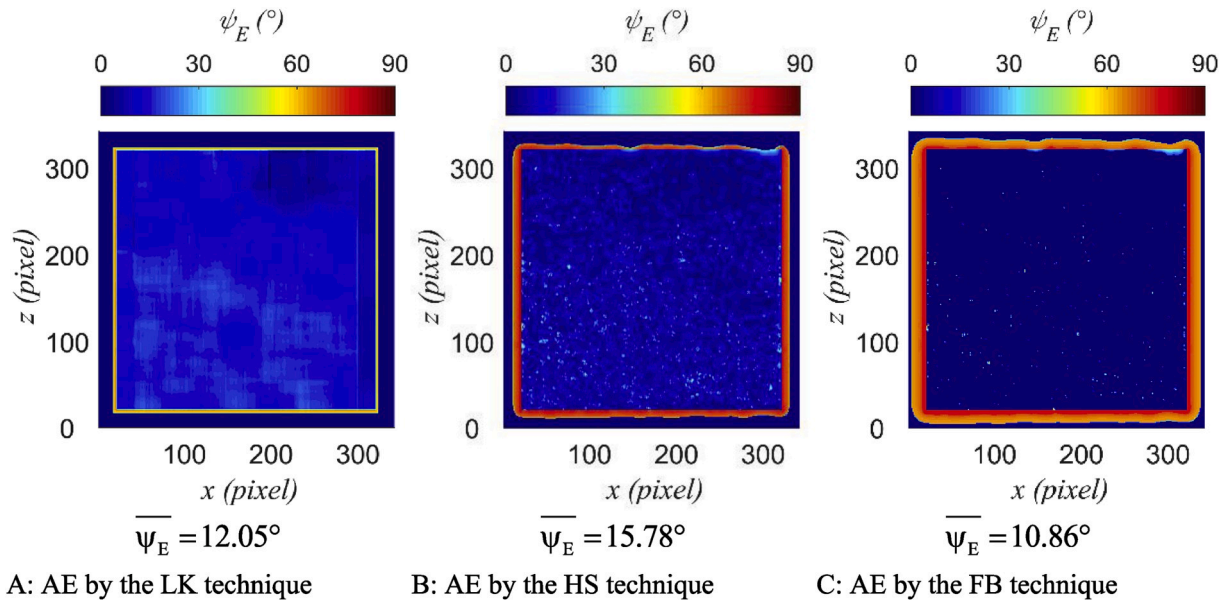


Fig. 12. Distributions of angular errors from the LK, HS and FB techniques. AE indicates the angular error.

growth, shrink and breakup due to the pressure variations and advection of large coherent structures in the breaking roller. Addressing these issues is beyond the scope of this paper, and it is worthwhile to perform a detailed study on the turbulence measurements in the breaking surges using optical flow techniques.

7. Conclusion

In a breaking surge, unsteady air bubble entrainment takes place in the roller. Monophase flow instrumentations, as well as traditional gas-liquid flow metrology, cannot be used in the highly aerated roller region. In this study, three optical flow techniques were tested in a breaking surge with the bore Froude number $Fr_1 = 2.1$. These included the Lucas and Kanade (LK), Horn and Schunck (HS) and Farnback techniques (FB). Based upon ultra-high-speed video movies, a comparison among the three optical flow techniques and literature showed that the FB technique was a most suitable optical flow method to obtain ensemble averaged two-dimensional velocity fields in the air-water roller region, except next to the air-water flow boundaries. The bore generation by a rapid gate closure showed a highly-unsteady complicated velocity field, with substantial free-surface deformations, wave breaking and formation of large coherent structures before the surge detached from the gate region. Further upstream, i.e. at $x = 8.5$ m, the surge propagated as a breaking bore in translation and the air-water optical flow and image processing data showed a marked shear region with a recirculation above. The surging breaking wave presented air-water flow features

comparable to a hydraulic jump, with fluid entrainment in the shear layer region. The present data implied an air-to-water velocity ratio about 4–5.

It is believed that the present result brings new information on the fluid characteristics of highly-aerated breaking surges. The data revealed the turbulent nature of some complicated two-phase flow with large-scale turbulence. The results will need further developments. For example, experimental studies with larger Froude numbers could be undertaken, as well as some comparative analysis with phase-detection probe data, despite the metrology challenges discussed by Ref. Leng and Chanson [28]. Detailed numerical modelling of breaking bores may also be another research direction and the amount of data collected up to date provides a calibration database.

Declaration of competing interest

The authors have no conflict of interest nor vested interests.

Acknowledgments

The authors thank Professor Pierre Lubin (University of Bordeaux, France) for assistance the physical experiments, Dr Gangfu Zhang (WSP, Australia) and Dr Matthias Kramer (University of New South Wales Canberra, Australia) for helpful discussions, and Mr Jason Van Der Gevel and Stewart Matthews (The University of Queensland, Australia) for technical assistance.

Appendix C. Supplementary data

Supplementary data to this article can be found online at <https://doi.org/10.1016/j.flowmeasinst.2020.101710>.

APPENDIX A. Optical flow algorithms

A.1. Lucas-Kanade technique

The Lucas and Kanade technique, widely adopted in the computer vision community, has been developed to compute optical flow and parametrize apparent motion [64]. It assumes that the optical flow is constant in a local neighbourhood of the pixel between two nearby frames, so called the brightness constancy constraint assumption:

$$I(x_{im}, y_{im}, t_{im}) = I(x_{im} + dx_{im}, y_{im} + dy_{im}, t_{im} + dt_{im}) \quad (\text{A.1})$$

where I is brightness intensity ranged from 0 to 256 in an 8-bit grey level image, x_{im} and y_{im} are the Cartesian image plane coordinates, dx_{im} and dy_{im} are the displacements in the image plane, and t_{im} and dt_{im} are the time and time change between two frames. The right-hand-side of Equation (A.1) is rewritten using Taylor Series, and simplified to a form of the temporal and spatial gradients of brightness intensity:

$$I(x_{im}, y_{im}, t_{im}) = I(x_{im}, y_{im}, t_{im}) + \frac{\partial I}{\partial x}(x_{im} + dx_{im} - x_{im}) + \frac{\partial I}{\partial y}(y_{im} + dy_{im} - y_{im}) + \frac{\partial I}{\partial t}(t_{im} + dt_{im} - t_{im}) \quad (\text{A.2})$$

$$I_x u_{im} + I_y v_{im} = -I_t \quad (\text{A.3})$$

where I_x , I_y , and $I_t = \partial I / \partial x$, $\partial I / \partial y$ and $\partial I / \partial t$, and u_{im} and v_{im} are the optical flow velocity vectors in the image plane. In a local neighbourhood of n pixels, assuming small and constant displacement between two adjacent frames, additional constraints can be obtained in matrix form: $A_{im} d_{im} = b_{im}$, where

$$A_{im} = \begin{bmatrix} I_{x,1} & I_{y,1} \\ I_{x,2} & I_{y,2} \\ \vdots & \vdots \\ I_{x,n} & I_{y,n} \end{bmatrix}, \quad d_{im} = \begin{bmatrix} u_{im} \\ v_{im} \end{bmatrix}, \quad b_{im} = \begin{bmatrix} I_{t,1} \\ I_{t,2} \\ \vdots \\ I_{t,n} \end{bmatrix} \quad (\text{A.4})$$

Above equation is overdetermined. The local optical flow vector is obtained using the least squared principles:

$$d_{im} = (A_{im}^T A_{im})^{-1} A_{im}^T b_{im} \quad (\text{A.5})$$

Namely, Equation (A.5) may be rewritten to a 2-by-2 matrix system as:

$$\begin{bmatrix} u_{im} \\ v_{im} \end{bmatrix} = \begin{bmatrix} \sum I_{x,i}^2 & \sum I_{x,i}I_{y,i} \\ \sum I_{x,i}I_{y,i} & \sum I_{y,i}^2 \end{bmatrix}^{-1} \begin{bmatrix} -\sum I_{x,i}I_{t,i} \\ -\sum I_{y,i}I_{t,i} \end{bmatrix} \quad (\text{A.6})$$

The crucial part of above computation is the invertibility of the matrix $A_{im}^T A_{im}$, but not for a local neighbourhood with no spatial and temporal gradient. One way to demonstrate the quality of the matrix inversion is to acquire the two eigenvalues, λ_1 and λ_2 . If more than one of them are small, the local neighbourhood may have a noise issue. If λ_1/λ_2 is too large, this indicate an edge region. Ideally, λ_1 and λ_2 are large, and have similar values.

Owing to the high frame rate in the present study (22,607 fps), high-frequency noise might exist between two nearby frames. The Gaussians smooth method was applied to remove the temporal noise from the Lucas-Kanade optical flow. In the present case of grayscale images, frame was smoothed by convolving the original images with Gaussian kernels of respective standard deviations:

$$G(x_{im}, y_{im}) = I(x_{im}, y_{im})g(x_{im}, y_{im}) \quad (\text{A.7})$$

$$g(x_{im}, y_{im}) = \frac{1}{\sqrt{2\pi\sigma^2}} \exp\left(-\frac{x_{im}^2 + y_{im}^2}{2\sigma^2}\right) \quad (\text{A.8})$$

where I is the brightness data and σ is the standard deviations of Gaussian.

A.2. Horn-Schunck technique

The Horn-Schunck technique is the first variational approach to estimate optical flow by solving a minimization problem. The brightness constancy constraint assumption, defined in Equation (A.1), is still valid, with additional global smoothness constraint introduced to address the constraint indeterminacy (aperture problem). Equation (A.3) may be expressed as the first optical flow constrain equation:

$$v_{im} = -\frac{I_x}{I_y} - \frac{I_x}{I_y} u_{im} \quad (\text{A.9})$$

Equation (A.9) is illustrated in Figure A1. The optical flow vector coordinates (u_{im}, v_{im}) may be located at any point along the linear equation, and the optical flow vector can be written as a sum of normal and parallel flow vectors:

$$v_{HS} = d_{HS} + P_{HS} \quad (\text{A.10})$$

There is not enough information to obtain the parallel flow vector $\overrightarrow{P_{HS}}$. The normal flow vector, representing the smallest motion, equals the magnitude of the motion in the gradient direction:

$$d_{HS} = -\frac{I_t}{\sqrt{I_x^2 + I_y^2}} \quad (\text{A.11})$$

The brightness constancy constrain cannot determine the optical flow vector. A smoothness assumption is made. This is, the optical flow velocity field of the image brightness varies smoothly, which implies the small motion in the neighbouring points. The measure of the smoothness is the sum of the squares of the two velocities gradients. Then goal is to minimize the two errors caused by the brightness constancy constrain and the global smoothness constrains, formulated as:

$$\iint (I_x u_{im} + I_y v_{im} + I_t)^2 + \alpha^2 (\|\nabla u_{im}\|^2 + \|\nabla v_{im}\|^2) dx_{im} dy_{im} \quad (\text{A.12})$$

where α is the regularisation constant, $\nabla = \partial/\partial x$ is the spatial gradient operator, and $\|\cdot\|$ is the norm operator. Note that the parameter α was introduced to control the weight of the smoothness term [30]; and larger α indicated a smoother flow. Solving Euler-Lagrange equations, the minimization of above functions gives:

$$\begin{aligned} I_x(I_x u_{im} + I_y v_{im} + I_t) &= \alpha^2 \Delta(u_{im}) \\ I_x(I_x u_{im} + I_y v_{im} + I_t) &= \alpha^2 \Delta(v_{im}) \end{aligned} \quad (\text{A.13})$$

where $\Delta = \partial^2/\partial x^2 + \partial^2/\partial y^2$ is the Laplace operator. The Laplacian is numerically approximated using the weighted average from an eight neighbours, as well as estimating the partial derivatives of the brightness intensity between two consecutive frames:

$$I_{x,y,t} \approx \frac{1}{4} [(I_{i+1,j+1,k+1} - I_{i+1,j,k+1}) + (I_{i,j+1,k+1}, I_{i,j,k+1}) + (I_{i+1,j+1,k} - I_{i+1,j,k}) + (I_{i,j+1,k} - I_{i,j,k})] \quad (\text{A.14})$$

$$\begin{aligned} \bar{u}_{im,i,j,k} &= \frac{1}{6} (u_{im,i-1,j,k} + u_{im,i+1,j,k} + u_{im,i,j-1,k} + u_{im,i,j+1,k}) \\ &+ \frac{1}{12} (u_{im,i-1,j-1,k} + u_{im,i+1,j-1,k} + u_{im,i-1,j+1,k} + u_{im,i+1,j+1,k}) \end{aligned} \quad (\text{A.15})$$

where all the paramters and index are defined in Figures A1B and A.1C.

Using the approximation introduced above, the constraint equation can be rewritten as:

$$\begin{aligned} I_x(I_x u_{im} + I_y v_{im} + I_t) &= \alpha^2 (\bar{u}_{im} - u_{im}) \\ I_x(I_x u_{im} + I_y v_{im} + I_t) &= \alpha^2 (\bar{v}_{im} - v_{im}) \end{aligned} \quad (\text{A.16})$$

where \bar{u}_{im} and \bar{v}_{im} are the weighted average optical flow velocities. This set of equation can be solved by Gauss-Jordan elimination, but it is too computationally expensive. Alternatively, it can be obtained using an iterative scheme. The optical flow velocities from $(n+1)^{th}$ iteration can be computed using the estimated partial derivative and weighted average optical flow velocities from n^{th} iteration:

$$u_{im}^{n+1} = \bar{u}_{im} - I_x \frac{I_x \bar{u}_{im} + I_y \bar{v}_{im} + I_t}{\alpha^2 + I_x^2 + I_y^2}$$

$$v_{im}^{n+1} = \bar{v}_{im} - I_y \frac{I_x \bar{u}_{im} + I_y \bar{v}_{im} + I_t}{\alpha^2 + I_x^2 + I_y^2}$$
(A.17)

where index $n+1$ means the next iteration. The interaction process starts with two optical flow velocities equal to 0. Then, a new set of velocities for next iteration is assumed as the velocities obtained from the previous time-step. Prior to the differentiation of the Horn-Schunck technique, the image sequence was smoothed using the DoG method, as presented in the previous section. The low-pass effect of the DoG method was aimed to remove high-frequency electronic noise.

The major limitation of the Horn-Schunck technique is the smoothness assumption. It can provide robust results for only small and continuous motion. In the presence of discontinuous displacements, the smoothness assumption is no longer valid because of the large spatial and temporal gradients. In the present study, the propagation of the breaking bore was considered having small motion for the ultrahigh frame rate of 22,607 fps.

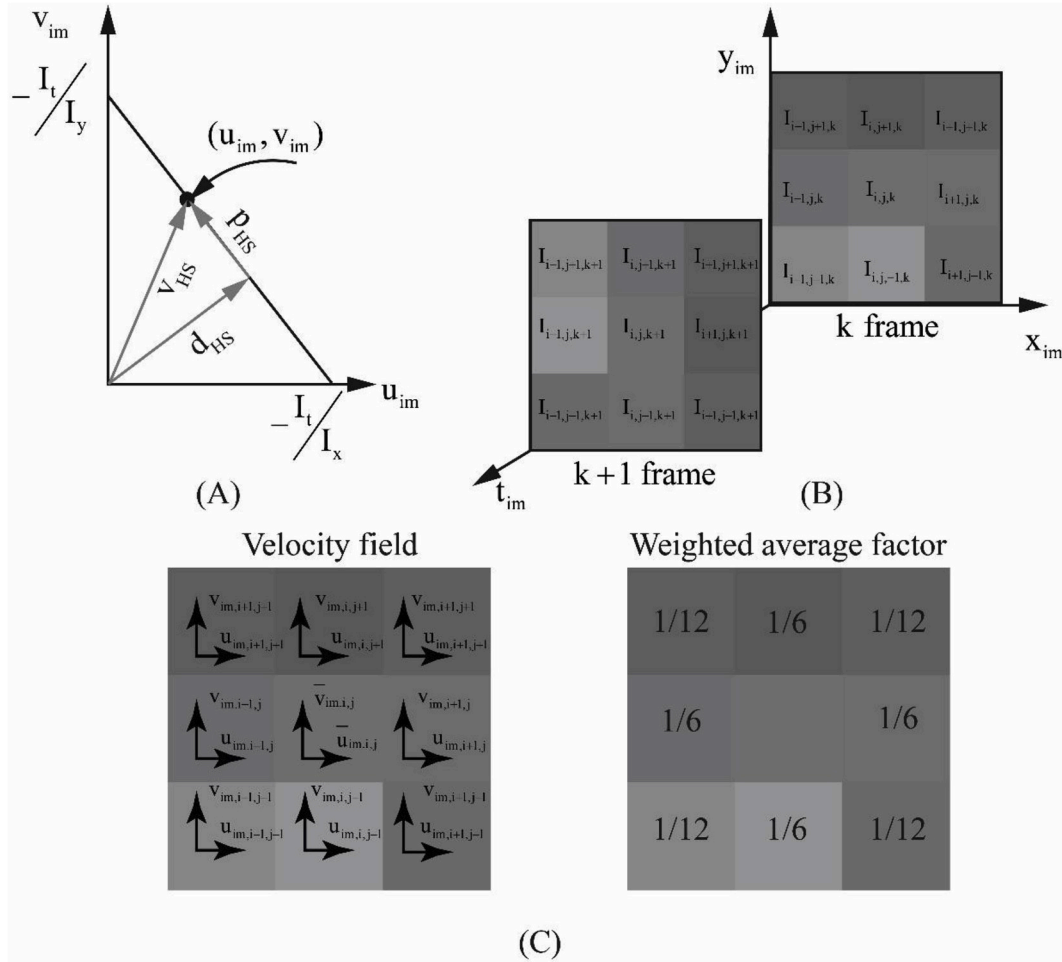


Fig. A.1. Definition sketches of the Horn-Schunck technique - (A) brightness constancy constrain equation; (B) numerical estimation of partial derivatives of the brightness between two consecutive frames, where row index i corresponds to the x direction in an image, column index j lies to the y direction in an image, and index k means k frame in the video; (C) the Laplacian estimation of two optical flow velocities using weighted averaged method from eight neighbouring points.

A.3. Farneback technique

Farneback [46,47] proposed a variational optical flow technique. It locally estimates the optical flow at each pixel of two consecutive frames by quadratic polynomials. The first image can be expressed as:

$$f_1(x_{im}, y_{im}) \cong a_1 + a_2x + a_3y + a_4x_{im}^2 + a_5y_{im}^2 + a_6x_{im}y_{im}$$
(A.18)

where a_1, a_2, a_3, a_4, a_5 and a_6 are the polynomial coefficients. Equation (A.18) can be rewritten as:

$$f_1(X_{im}) \cong X_{im}^T A_{f1} X_{im} + b_{f1}^T X_{im} + c_{f1}$$
(A.19)

where

$$X_{im} = \begin{bmatrix} x_{im} \\ y_{im} \end{bmatrix}, \quad A_{f1} = \begin{bmatrix} a_4 & a_6/2 \\ a_6/2 & a_5 \end{bmatrix}, \quad b_{f1} = \begin{bmatrix} a_2 \\ a_3 \end{bmatrix}, \quad c_{f1} = a_1 \quad (\text{A.20})$$

The second image is the translation of the first image by a displacement vector d_f :

$$\begin{aligned} f_2(X_{im}) &= f_1(X_{im} - d_f) \\ &= (X_{im} - d_f)^T A_{f1} (X_{im} - d_f) + b_{f1}^T (X_{im} - d_f) + c_{f1} \\ &= X_{im}^T A_{f1} X_{im} + (b_{f1} - 2A_{f1}d_f)^T X_{im} + d_f^T A_{f1} d_f - b_{f1}^T d_f + c_{f1} \\ &= X_{im}^T A_{f2} X_{im} + b_{f2}^T X_{im} + c_{f2} \end{aligned} \quad (\text{A.21})$$

Equation (A.21) yields:

$$A_{f2} = A_{f1} \quad (\text{A.22})$$

$$b_{f2} = b_{f1} - 2A_{f1}d_f \quad (\text{A.23})$$

$$c_{f2} = d_f^T A_{f1} d_f - b_{f1}^T d_f + c_{f1} \quad (\text{A.24})$$

For a non-singular A_{f1} , Equation (A.23) gives the solution of the displacement vector:

$$d_f = \frac{1}{2} A_{f1}^{-1} (b_{f1} - b_{f2}) \quad (\text{A.25})$$

It is unrealistic to assume a polynomial representing a global translation. Therefore, a local constrain based on Equation (A.23) is given:

$$A_f(X_{im})d_f(X_{im}) = \Delta b_f(X_{im}) \quad (\text{A.26})$$

where

$$A_f(X_{im}) = \frac{A_{f1}(X_{im}) + A_{f2}(X_{im})}{2} \quad (\text{A.27})$$

$$\Delta b_f(X_{im}) = -\frac{1}{2} (b_{f2}(X_{im}) - b_{f1}(X_{im}))$$

Pointwise results encompass too much noisy [46], so it considers to minimize the sum of the local constrains for all the pixel in a neighbourhood:

$$\sum_{\Delta X_{im} \in \text{local}} w_f(\Delta X_{im}) \|A_f(X_{im} + \Delta X_{im})d_f(X_{im}) - \Delta b_f(X_{im} + \Delta X_{im})\|^2 \quad (\text{A.28})$$

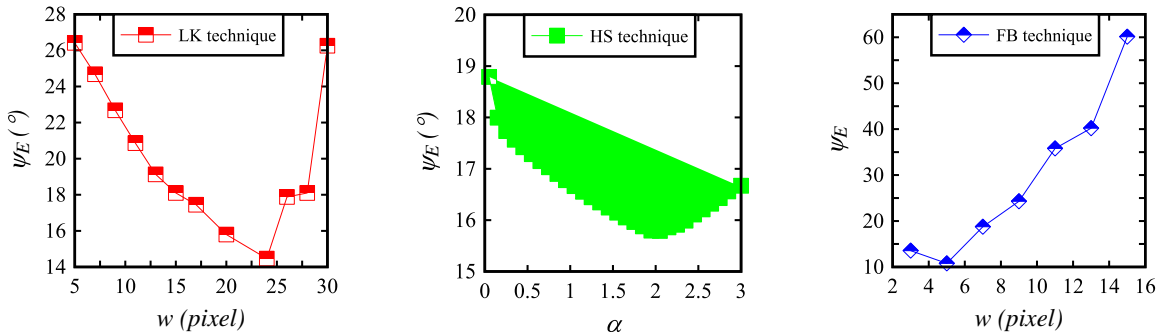
where w_f is a weight function over the neighbourhood. The minimization gives:

$$d_f(X_{im}) = \left(\sum w_f A_f^T A_f \right)^{-1} \sum w_f A_f^T \Delta b_f \quad (\text{A.29})$$

The above displacement vector can be solved using an iterative scheme. The iteration process starts with the displacement vector equal to zero. The estimated displacements from an iteration are used as the inputs in the next iteration. It usually takes 3 to 5 iterations until convergence.

APPENDIX B. Error analysis on parameters in optical flow techniques

Angular error may be an indicator to determine some key parameters in optical flow techniques, including the regularisation constant α in the HS technique, and sliding window size (w) in the LK and FB technique, as presented in Figure B1. For the optical flows obtained from the breaking surge, $w = 22$, $\alpha = 2$ and $w = 5$ were adopted for the LK, HS and FB technique respectively. Traditionally, the regularisation factor was expected to be approximately equal to 1. Herein, $\alpha = 2$ might turned into an over-smoothed optical flow field.



A: window size from LK technique

B: α from HS technique

C: window size from FB technique

Fig. B.1. Average angular error as a function of key parameters in optical flow techniques.2

The relationships between average angular error and displacement are presented in Figure B2, showing that larger displacement resulted in greater inaccuracy of optical flow field. For a small displacement, the measure of angular error suggested that the FB technique outperformed in the air-water flow. In the present study, the ultra-high-speed videos were analysed using 22,607 fps, thus holding the assumption of small displacement between consecutive frames, and minimising the angular error.

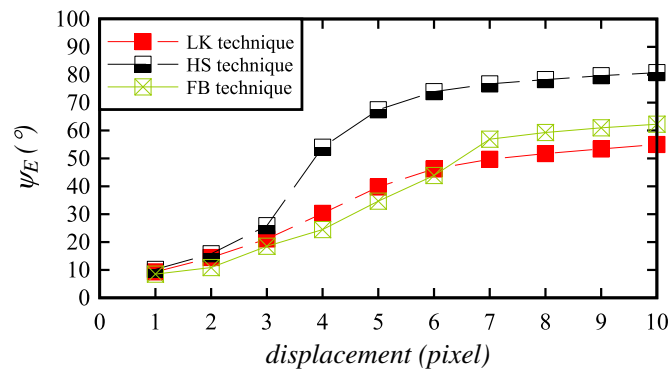


Fig. B.2. average angular error with a function of horizontal displacement. 3

References

- G.M. Quénot, J. Pakleza, T.A. Kowalewski, Particle image velocimetry with optical flow, *Exp. Fluid* 25 (3) (1998) 177–189.
- T. Corpetti, E. Memin, P. Perez, Dense parametric estimation of fluid flows, *IEEE Trans. Pattern Anal. Mach. Intell.* 24 (3) (2002) 1–5.
- T. Liu, L. Shen, Fluid flow and optical flow, *J. Fluid Mech.* 614 (2008) 253–291.
- J. Yuan, C. Schnörr, E. Mémin, Discrete orthogonal decomposition and variational fluid flow estimation, *J. Math. Imag. Vis.* 28 (1) (2007) 67–80.
- D. Heitz, E. Mémin, C. Schnörr, Variational fluid flow measurements from image sequences: synopsis and perspectives, *Exp. Fluid* 48 (3) (2010) 369–393.
- D.B. Bung, D. Valero, Optical flow estimation in aerated flows, *J. Hydraul. Res.* 54 (5) (2016) 575–580.
- M. Kramer, H. Chanson, Optical flow measurements in aerated spillway flows: validation and discussion on sampling/processing parameters, in: *Experimental Thermal and Fluid Science*, vol. 103, Elsevier Inc., 2019, pp. 318–328.
- G. Zhang, H. Chanson, Application of local optical flow methods to high-velocity free-surface flows: validation and application to stepped chutes, *Experimental Thermal and Fluid Science*, Elsevier 90 (July 2017) (2018) 186–199.
- P. Lubin, H. Chanson, Are breaking waves, bores, surges and jumps the same flow? *Environ. Fluid Mech.* 17 (1) (2017) 47–77, <https://doi.org/10.1007/s10652-016-9475-y>.
- D.H. Peregrine, I.A. Svendsen, Spilling breakers, bores and hydraulic jumps, *Proc. 16th International Conference on Coastal Engineering II* (30) (1978) 540–550.
- D.B. Coakley, P.M. Haldeman, D.G. Morgan, K.R. Nicolas, D.R. Penndorf, L. B. Wetzel, C.S. Weller, Electromagnetic scattering from large steady breaking waves, *Exp. Fluid* 30 (5) (2001) 479–487.
- R. Cointe, M.P. Tulin, A theory of steady breakers, *J. Fluid Mech.* 276 (1994) 1–20.
- H.G. Hornung, C. Willert, S. Turner, The flow field downstream of a hydraulic jump, *J. Fluid Mech.* 287 (1995) 299–316.
- C. Koch, H. Chanson, Turbulence measurements in positive surges and bores, *J. Hydraul. Res.* 47 (1) (2009) 29–40.
- A.J.C. Barré de Saint Venant, Théorie du Mouvement Non Permanent des Eaux, avec Application aux Crues des Rivières et à l'Introduction des Marées dans leur Lit, *Comptes Rendus des séances de l'Académie des Sciences*, Paris, France 73 (4) (1871) 147–154 (in French).
- A.J.C. Barré de Saint Venant, Théorie et Equations Générales du Mouvement Non Permanent des Eaux, avec Application aux Crues des Rivières et à l'Introduction des Marées dans leur Lit (2ème Note), in: *Comptes Rendus des séances de l'Académie des Sciences*, Paris, France, Séance 17 July 1871, vol. 73, 1871, pp. 237–240 (in French).
- T.B. Benjamin, M.J. Lighthill, On cnoidal waves and bores, *Proc. Royal Soc. of London, Series A, Math. & Phys. Sc.* 224 (1159) (1954) 448–460.
- D.H. Peregrine, Calculations of the development of an undular bore, *J. Fluid Mech.* 25 (1966) 321–330.
- B. Simon, Ph.D. thesis, Effects of Tidal Bores on Turbulent Mixing: a Numerical and Physical Study in Positive Surges, School of Civil Engineering, The University of Queensland, Brisbane, Australia, 2014, p. 259, pages & 7 movies.
- N. Khezri, Modelling Turbulent Mixing and Sediment Process beneath Tidal Bores: Physical and Numerical Investigations, Ph.D. thesis, School of Civil Engineering, The University of Queensland, Brisbane, Australia, 2014, p. 267.
- X. Leng, Study of Turbulence: the Unsteady Propagation of Bores and Surges, Ph.D. thesis, School of Civil Engineering, The University of Queensland, Brisbane, Australia, 2018, p. 364. pages & 2 Digital Appendices.
- X. Leng, B. Simon, N. Khezri, P. Lubin, H. Chanson, CFD modelling of tidal bores: development and validation challenges, *Coast Eng. J.* 60 (4) (2018) 423–436, <https://doi.org/10.1080/21664250.2018.1498211>.
- F. Benet, J.A. Cunge, Analysis of experiments on secondary undulations caused by surge waves in trapezoidal channels, *Journal of Hydraulic Research*, IAHR 9 (1) (1971) 11–33.
- H. Favre, Etude Théorique et Expérimentale des Ondes de Translation dans les Canaux Découverts, in: *Theoretical and Experimental Study of Travelling Surges in Open Channels*, Dunod, Paris, France, 1935 (in French).
- X. Leng, H. Chanson, Coupling between free-surface fluctuations, velocity fluctuations and turbulent Reynolds stresses during the upstream propagation of positive surges, bores and compression waves, *Environ. Fluid Mech.* 16 (4) (2016) 695–719, <https://doi.org/10.1007/s10652-015-9438-8> & digital appendix.
- H. Chanson, D. Reungoat, B. Simon, P. Lubin, High-frequency turbulence and suspended sediment concentration measurements in the garonne river tidal bore, *Estuar. Coast Shelf Sci.* 95 (2–3) (2011) 298–306, <https://doi.org/10.1016/j.ecss.2011.09.012>.
- D. Reungoat, P. Lubin, X. Leng, H. Chanson, Tidal bore hydrodynamics and sediment processes: 2010–2016 field observations in France, *Coast Eng. J.* 60 (4) (2018) 484–498, <https://doi.org/10.1080/21664250.2018.1529265>.
- X. Leng, H. Chanson, Two-phase flow measurements of an unsteady breaking bore, *Exp. Fluid* 60 (3) (2019), <https://doi.org/10.1007/s00348-019-2689-2>. Paper 42, 15 pages & 2 video movies.
- X. Leng, H. Chanson, Air-water interaction and characteristics in breaking bores, *Int. J. Multiphas. Flow* 120 (2019) 17, <https://doi.org/10.1016/j.ijmultiphaseflow.2019.103101>. Paper 103101.
- B.K. Horn, B.G. Schunck, Determining Optical Flow, Artificial Intelligence, Washington, D.C., United States, 1981, pp. 319–331.
- B. Lucas, T. Kanade, An iterative image registration technique with an application to stereo vision, *IJCAI* 81 (1) (1981) 674–679.
- H.H. Nagel, On the estimation of optical flow: relations between different approaches and some new results, *Artif. Intell.* 33 (3) (1987) 299–324.
- P. Anandan, Measuring Visual Motion from Image Sequences, PhD dissertation, University of Massachusetts, Amherst, USA, 1987.
- P. Anandan, A computational framework and an algorithm for the measurement of visual motion, *Int. J. Comput. Vis.* 2 (3) (1989) 283–310.
- D.J. Heeger, Optical flow using spatiotemporal filters, *Int. J. Comput. Vis.* 1 (1988) 279–302.
- D.J. Fleet, A.D. Jepson, Computation of component image velocity from local phase information, *Int. J. Comput. Vis.* 5 (1) (1990) 77–104.
- K. Wahn, A.M. Waxman, Contour evolution, neighborhood deformation and local image flow: curved surfaces in motion, *Int. J. Robot Res.* 134 (1985) 95–108.
- J.L. Barron, D.J. Fleet, S.S. Beauchemin, Performance of optical flow techniques, *Int. J. Comput. Vis.* 12 (1) (1994) 43–77.
- S. Baker, D. Scharstein, J.P. Lewis, S. Roth, M.J. Black, R. Szeliski, A database and evaluation methodology for optical flow, *Int. J. Comput. Vis.* 92 (1) (2011) 1–31.
- J.R. Bergen, P. Anandan, K.J. Hanna, R. Hingorani, Hierarchical Model-Based Motion Estimation, European Conference on Computer Vision, 1992, pp. 237–252.
- T. Brox, J. Malik, Large displacement optical flow: descriptor matching in variational motion estimation, *IEEE Transactions on Pattern Analysis and Machine Intelligence*, IEEE 33 (3) (2011) 500–513.
- E.H. Adelson, C.H. Anderson, J.R. Bergen, P.J. Burt, J.M. Ogden, Pyramid methods in image processing, *RCA Engineer* 29 (6) (1984) 33–41.

- [43] D. Sun, S. Roth, M.J. Black, Secrets of optical flow estimation and their principles, in: Proceedings of the IEEE Computer Society Conference on Computer Vision and Pattern Recognition, IEEE, 2010, pp. 2432–2439.
- [44] H. Zimmer, A. Bruhn, J. Weickert, L. Valgaerts, A. Salgado, B. Rosenhahn, H.-P. Seidel, Complementary optical flow, in: Energy Minimization Methods in Computer Vision and Pattern Recognition, Springer-Verlag Berlin Heidelberg 2009, Bonn, Germany, 2009, 207–220–220.
- [45] M.V. Srinivasan, Generalized gradient schemes for the measurement of two-dimensional image motion, *Biol. Cybern.* 63 (6) (1990) 421–431.
- [46] G. Farnback, Polynomial expansion for orientation and motion estimation, PhD dissertation, 2002.
- [47] G. Farnback, Two-frame motion estimation based on polynomial expansion, in: Proceedings of the 13th Scandinavian Conference on Image Analysis, Pages, Springer-Verlag Berlin Heidelberg, 2003, pp. 363–370.
- [48] A. Bruhn, J. Weickert, Lucas/Kanade meets horn/schunck: combining local and global optic flow methods, *Int. J. Comput. Vis.* 61 (3) (2005) 211–231.
- [49] C.H. Anderson, P.J. Burt, G.S. van der Wal, Change detection and tracking using pyramid transform techniques, SPIE Conference on Intelligent Robotics and Computer Vision (1985) 72–78.
- [50] P.J. Burt, Fast filter transform for image processing, *Comput. Graph. Image Process.* 16 (1) (1981) 20–51.
- [51] P.J. Burt, Fast algorithms for estimating local image properties, *Comput. Graph. Image Process.* 21 (1983) 368–382.
- [52] H. Chanson, N.J. Docherty, Turbulent velocity measurements in open channel bores, *European Journal of Mechanics, B/Fluids*, Elsevier Masson SAS 32 (1) (2012) 52–58.
- [53] N. Khezri, H. Chanson, Undular and breaking bores on fixed and movable gravel beds, *J. Hydraul. Res.* 50 (4) (2012) 353–363.
- [54] C. Koch, H. Chanson, Turbulent mixing beneath an undular bore front, *J. Coast Res.* 244 (2008) 999–1007.
- [55] X. Leng, H. Chanson, Turbulent advances of a breaking bore: preliminary physical experiments, *Exp. Therm. Fluid Sci.* 62 (1) (2015) 70–77.
- [56] J.W. Hoyt, R.H.J. Sellin, Hydraulic jump as 'mixing layer', *Journal of Hydraulic Engineering*, ASCE 115 (12) (1989) 1607–1614.
- [57] H. Wang, Turbulence Air Entrainment in Hydraulic Jumps, Ph.D. thesis, School of Civil Engineering, The University of Queensland, Brisbane, Australia, 2014, p. 341, <https://doi.org/10.14264/uq.2014.542>, 341 pages & Digital appendices.
- [58] P.E. Dimotakis, Two-dimensional shear-layer entrainment, *AIAA J.* 24 (1986) 1791–1796.
- [59] G.L. Brown, The entrainment and large structure in turbulent mixing layers, in: Proceedings of the 5th Australasian Conference on Hydraulics and Fluid Mechanics, Christchurch, New Zealand, D. Lindley & A.J. Sutherland editors, 1974, pp. 352–359.
- [60] M. Mortazavi, V. Le Chenadec, P. Moin, A. Mani, Direct numerical simulation of a turbulent hydraulic jump: turbulence statistics and air entrainment, *J. Fluid Mech.* 797 (2016) 60–94.
- [61] C. Lin, S.C. Hsieh, L.J. Lin, K.A. Chang, R.V. Raikar, Flow property and self-similarity in steady hydraulic jumps, *Exp. Fluids* 53 (5) (2012) 1591–1616.
- [62] P. Lubin, S. Glockner, H. Chanson, Numerical simulation of a weak breaking tidal bore, *Mech. Res. Commun.* 37 (1) (2010) 119–121, <https://doi.org/10.1016/j.mechrescom.2009.09.008>.
- [63] S. Sun, X. Leng, H. Chanson, Rapid operation of a tainter gate: generation process and initial upstream surge motion, *Environ. Fluid Mech.* 16 (1) (2016) 87–100, <https://doi.org/10.1007/s10652-015-9414-3>.
- [64] M. Black, A. Jepson, EigenTracking: robust matching and tracking of articulated objects using a view based representation, *Int. J. Comput. Vis.* 26 (1) (1998) 63–84.
- E_p : volume-entrainment ratio (–)
- Fr_1 : bore Froude number, defined as: $Fr_1 = (V_1 + U)/\sqrt{gd_1}$ (–)
- G : Gaussian smooth method (–)
- g : gravity constant $g = 9.81 \text{ m s}^{-2}$ (–)
- I : brightness data (–)
- $I_{x,y,t}$: partial derivative of brightness data with respect to horizontal, vertical and time. ($\text{m}^{-1}, \text{m}^{-1}, \text{s}^{-1}$)
- Q : flow rate ($\text{m}^3 \text{ s}^{-1}$)
- N : number of pixels in image plane (–)
- N_v : number of videos (–)
- n : the n th frame in video (–)
- P_{HS} : parallel optical flow vector in the HS technique (px s^{-1})
- r : ratio of air velocity to water velocity (–)
- t_{im} : time between consecutive image (s)
- U : bore celerity (m s^{-1})
- u_{GT} : groud-truth horizontal optical flow (px s^{-1})
- u_{im} : horizontal optical flow in Cartesian image plane coordinate (px s^{-1})
- $u_{iv=n}$: the ensemble-averaged horizontal velocity using n videos (m s^{-1})
- V_{HS} : optical flow vector in the HS technique (px s^{-1})
- V_T : translating bore longitudinal velocity (m s^{-1})
- V_x : longitudinal velocity (m s^{-1})
- V_z : vertical velocity (m s^{-1})
- V_I : average velocity in initial flow (m s^{-1})
- v_{GT} : groud-truth vertical optical flow (px s^{-1})
- v_{im} : vertical optical flow in Cartesian image plane coordinate (px s^{-1})
- $v_{iv=n}$: the ensemble-averaged vertical velocity using n videos (m s^{-1})
- w : window size of local neighbourhood of the LK technique (px)
- w_f : a weight function over the neighbour in the FB technique (–)
- X_{im} : location matrix of the FB technique in a local neighbourhood (px)
- x : longitudinal direction in channel flow (m)
- x_{gate} : longitudinal location at downstream gate (m)
- x_{im} : x coordinate in Cartesian image plane coordinate (px)
- x_{toe} : longitudinal location of roller toe (m)
- y : transverse direction in channel flow (m)
- y_{im} : y coordinate in Cartesian image plane coordinate (px)
- $y_{UB, LB}$: the vertical distances of upper and lower bounds (m)
- z : vertical direction in channel flow (m) Greek letters
- α : regularisation constant in the HS technique (–)
- dt_{im} : time between consecutive frames (s^{-1})
- dx_{im} : apparent motion in optical flow estimations between two frames (px)
- $\lambda_{1,2}$: eigenvalues in the LK technique (–)
- σ : standard deviations of Gaussian (px)
- Ψ_E : Angular errors (°) Abbreviation
- ADM: acoustic displacement meter
- ADV: acoustic Doppler velocimetry
- BIV: bubble image velocimetry
- DNS: direct numerical simulation
- DOF: depth of field
- FB: Farnback optical flow technique
- LDA: laser Doppler velocimetry
- LK: Lucas and Kanade optical flow technique
- HS: Horn and Schunck optical flow technique
- PIV: particle image velocimetry

Notation

- A_f : symmetric second-order coefficient matrix in the FB technique (–)
- A_{im} : spatial derivative matrix of brightness data in a local neighbourhood of the LK technique (m^{-1})
- a : polynomial coefficients in the FB technique (–)
- b_f : first-order coefficient matrix in the FB technique (–)
- b_{im} : temporal derivative matrix of brightness data in a local neighbourhood of the LK technique (s^{-1})
- $C_{threshold1,2}$: thresholds in image processing technique (–)
- c_f : constant term in polynomial expansion of the FB technique (–)
- d_f : displacement vector in the FB technique (px)
- d_{HS} : normal optical flow vector in the HS technique (px s^{-1})
- d_{im} : optical flow matrix of the LK technique in a local neighbourhood (–)
- d_I : initial flow depth (m)
- EE: measure of optical flow variation (–)

Rui Shi is a Ph.D. research student at the University of Queensland. His research is focused on breaking surges and bores, encompassing experimental investigations and computational fluid dynamics (CFD) modelling of the air-water flow regions.

Xianqian Leng is a postdoctoral research fellow at the University of Queensland. Her research interests include experimental investigations of unsteady rapidly-varied open channel flows, computational fluid dynamics (CFD) modelling of steady and unsteady open channel flows, and field investigations of tidal bores. She authored 52 peer-reviewed papers, including 25 international scientific journal articles.

Hubert Chanson is a Professor in Civil Engineering, Hydraulic Engineering and Environmental Fluid Mechanics at the University of Queensland, Australia. His research interests include design of hydraulic structures, experimental investigations of two-phase flows, applied hydrodynamics, hydraulic engineering, water quality modelling, environmental fluid mechanics, estuarine processes and natural resources. His publication record includes over 1100 international refereed papers and several books, and his work was cited more than 4850 times (WoS) to 18,500 times (Google Scholar) since 1990. In 2019, his h-index was 37 (WoS), 43 (Scopus) and 67 (Google Scholar).

ON OPTICAL FLOW TECHNIQUES APPLIED TO BREAKING SURGES - SUPPLEMENTARY MATERIAL

By Rui SHI, Xinqian LENG and Hubert CHANSON

Sensitivity Analysis on Ensemble-Averaged Technique

C.1 - Presentation

A breaking surge is a highly unsteady turbulent physical process, associated with intensive air-entrainment, advection of large coherent structures and large free surface deformation. Instantaneous and time-averaged flow properties were meaningless in unsteady flow (Bradshaw 1971). Following previous studies (Docherty and Chanson 2012), an ensemble-averaged technique was used to obtain the flow velocities in the breaking surges. Herein, a sensitivity analysis was conducted in terms of the number of high-speed video records required to achieve reliable ensemble-averaged instantaneous optical flow velocity field, using a computationally cost-effective algorithm, the Lucas and Kanade technique (LK). The sensitivity analysis aimed to determine a reasonable number of repetitions required for obtaining meaningful ensemble-averaged optical flow fields.

C.2 - Results

Figure C.1 compares the ensemble-average instantaneous longitudinal velocity fields of 1, 5, 10, 20 and 23 videos using the LK technique. Some common features were shared by all velocity results in Figure C.1. The optical flow technique was able to detect a detailed optical flow velocity field in the two-phase air-water flow region and next to the free surface. Limited information in the clear water region was achieved because of constant brightness change. The bore roller formed immediately behind the toe, with a relatively higher velocity (Figure C.1, green area with $V_x/V_1 = -0.3$ to -0.4) in the bore front region compared with further downstream of the breaking roller (Figure C.1, green area with $V_x/V_1 = -0.1$ to -0.2). The initially steady flow travelled in the opposite direction of the roller propagation with a constant water velocity roughly equal to $+0.5$ m/s. It impinged at the roller toe with air intensely entrained into the roller. An air-water shear region developed, as shown by the large blue region between the bore and clear water regions in Figure C.1. A few errors, highlighted as the scattered dots in the bottom and top of the image plane, might be caused by the ambient light and inevitable reflections.

SHI, R., LENG, X., and CHANSON, H. (2020). "On Optical Flow Techniques applied to Breaking Surges." *Flow Measurement and Instrumentation*, Vol. 72, Paper 101710, 18 pages & Supplementary material (4 pages) (DOI: 10.1016/j.flowmeasinst.2020.101710) (ISSN 0955-5986).

Differences in the ensemble-averaged optical flow velocity field were seen with an increasing number of video movies. The ensemble-averaged instantaneous velocity fields based upon 1 and 5 videos (Figures C.1 A and B) presented a significant number of velocity discontinuity (red dots), compared to the other results. The number of erroneous data, highlighted as scattered dot areas with large absolute value of the velocities, decreased with an increasing number of video movies. The boundaries between the free-surface and shear region tended to become smoother in the velocity fields of more than 10 videos. The errors outside of the air-water flow region were drastically reduced in the ensemble-averaged velocity fields based upon 23 video movies. Overall, the comparison between the velocity fields from 1 to 23 videos showed a significant improvement with increasing number of video movies, and similar velocity distributions were observed for the ensemble-averaged optical flow velocity fields based upon 20 and 23 videos.

Figure C.2 presents typical cross-sectional profiles extracted at two longitudinal locations ($x-x_{toe}/d_1 = 2.2$ and 4.2) from Figure C.1. The results showed relatively larger velocity fluctuations for 1 video and 5 videos. The profiles become smoother with an increase in video number, especially when the number of video larger than 20. In summary, the results suggested that a minimum number of 20 videos was able to provide a reasonable optical flow field. In the current study, 23 videos were used to obtain the two-dimensional optical flow fields.

C3. REFERENCES

- Bradshaw, P. (1971). "An Introduction to Turbulence and its Measurement." Pergamon Press, Oxford, UK, The Commonwealth and International Library of Science and technology Engineering and Liberal Studies, Thermodynamics and Fluid Mechanics Division, 218 pages.
- Docherty, N. J., and Chanson, H. (2012). "Physical Modeling of Unsteady Turbulence in Breaking Tidal bores." *journal of hydraulic engineering*, 138(5), 412–419.

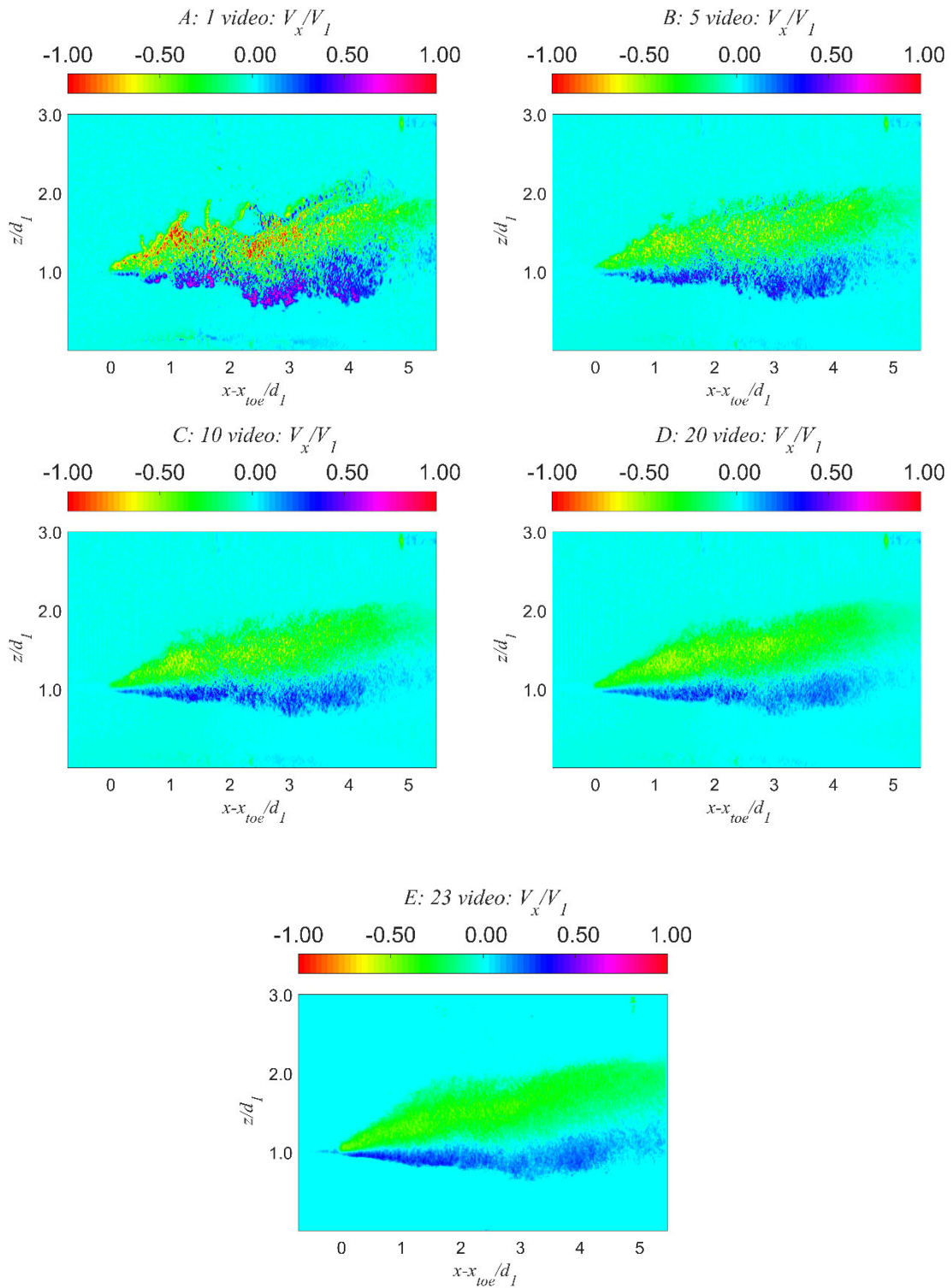
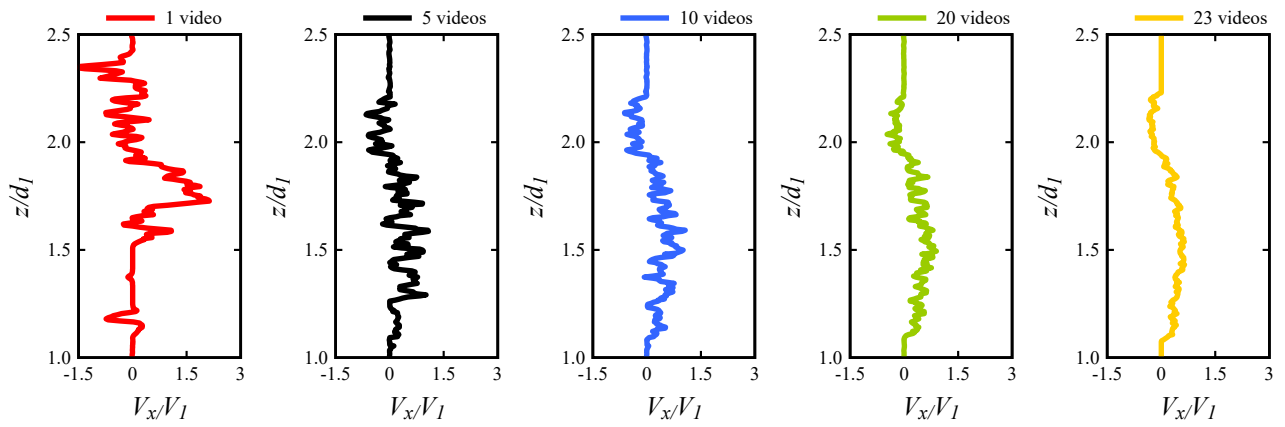
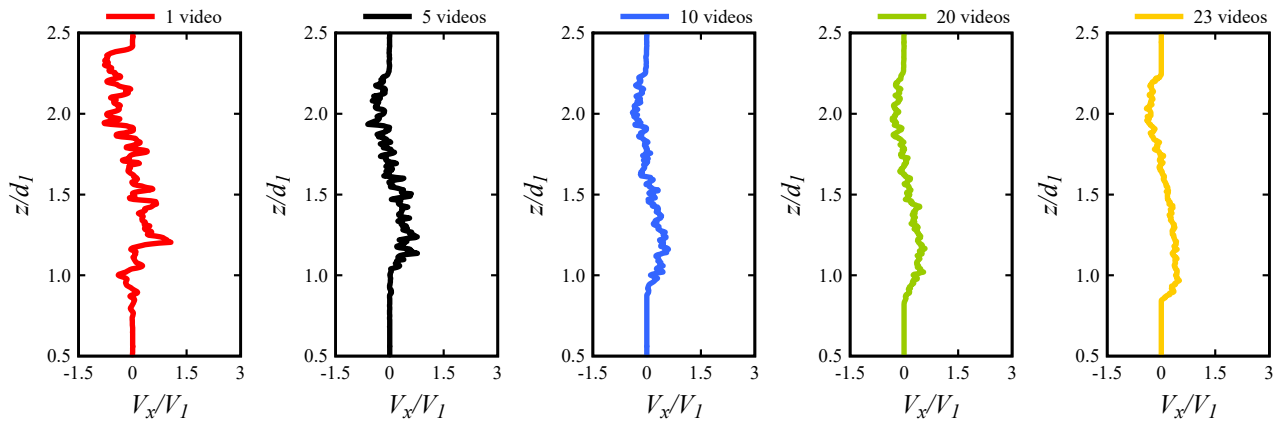


Figure C.1 - Dimensionless ensemble-averaged longitudinal optical flow data based on 1, 5, 10, 20 and 23 high-speed video movies using the LK technique - All the plots have the same legend - Flow conditions: initial flow from left to right, the bore propagation from right to left, $x = 8.5$ m, $Q = 0.101$ m³/s, $Fr_1 = 2.1$. Note that the positive longitudinal direction corresponds to the initial flow direction.



A: velocity distributions at $x-x_{toe}/d_1 = 2.2$



B: velocity distributions at $x-x_{toe}/d_1 = 4.2$

Figure C.2 - Dimensionless ensemble-averaged velocity profiles at different longitudinal locations: $x-x_{toe}/d_1 = 2.2$ and 4.4.